A Multi-Level Home Energy Management System (HEMS) for DC-Microgrids

Xin Lin, *Member*, *IEEE,* Ramon Zamora, *Senior Member*, *IEEE*, Yazhou Jiang, *Member*, *IEEE*, Gang Chen, and Anurag K. Srivastava, *Fellow*, *IEEE*

***Abstract*—It is essential for Home Energy Management Systems (HEMSs) to minimize the system operating cost while maintaining the user comfort under forecasting uncertainties of solar and electricity load demand. However, the existing HEMS excessively relies on a single battery system and may not effectively assess user comfort. To this end, a hierarchical HEMS, i.e., system- and local-level, is proposed in this article to coordinate the dispatch of home resources including battery energy storages and supercapacitors (SC). The system-level HEMS consists of long-term (LT) and short-term (ST) optimization based on Model Predictive Control (MPC). The LT optimization optimizes resource dispatch by using forecasted load and solar generation to minimize house operating costs and maximize the user comfort. The ST layer one is proposed to track the optimal power scheduling to minimize the cost error, refine the dispatch of resources and ensure a safe operational level of hybrid energy storage systems including the SC. The SC is employed to compensate the transient power and alleviate the battery degradation effects. The local-level HEMS is used to achieve DC voltage restoration, power sharing, voltage recovery of SC and state of charge (SoC) balance between batteries. The interaction between system- and local-level is also discussed. By using the dataset from NREL and Ameren Illinois Company, the test results show that this methodology can potentially reduce the system operating cost by 4.3500%, 7.7600%, and 37.7253% compared to the other single and multi-layer HEMSs.**

***Index Terms*—Consensus algorithm, DC home microgrid, degradation cost model, home energy management system, hybrid energy storage system, power sharing, SoC balance, user comfort.**

I. Introduction

RECENTLY, approximately one third of energy usage is consumed in the residential sector. However, about 89.3 % electricity is generated by carbon-intense resources [1]. Utilization of these types of energy resources including coal, natural gas, etc. have negative impacts on the environment such as the rising temperature due to climate change and degraded air quality. To reduce energy consumption, improve energy efficiency, and alleviate environmental concerns, small-scale power systems including renewable energy source (RES) and energy storage system (ESS) has emerged as an alternative solution for residential buildings. These power systems are also defined as home microgrid [2]. So far, a large number of DC electrical loads have applied in houses, such as lights and air conditioners. In addition, the power generated by photovoltaic (PV) systems has DC nature. DC-based microgrids can be better used in housing scenarios, which can improve energy efficiency and simplify power conversion [3]. In a DC home microgrid with heterogeneous sources and uncertain load demand, the home energy management system (HEMS) plays a significant role in optimizing energy usage to maximize the welfare through coordinated power supply from various energy resources and decision support for the customers' demand [4].

Many existing works have studied the HEMS [5]–[7]. For example, the HEMS methods in [5]–[7] are proposed to optimize the energy usage and customers' comfort level. However, these methods do not consider RESs. In [8], a HEMS that incorporates hybrid energy sources is designed for smart homes. The proposed method enables the development of optimal appliance scheduling to reduce the energy cost under various electric tariffs. A day-ahead optimization approach in [9] is developed to optimize the consumers' economy and comfort levels. In [10], a hybrid energy management that includes day-ahead optimization and rule-based priority method is proposed to optimize the usages of appliances, electric vehicle and battery in a smart solar house. The research works in [8]–[10] are carried out on the premise that the prediction of RES generation is accurate. However, the uncertainty caused by weather conditions may decrease the predictive accuracy [11].

Research works in [12]–[14] have taken the uncertainties into account in presented HEMS. However, these methods minimize electricity costs by hourly optimal load scheduling. The intermittent power generation of RES and the randomness of household load usage can lead to a power mismatch between hourly power scheduling and intra-hourly power usage. To overcome this drawback, some studies propose multi-level optimization framework [15]–[21]. For example, a two-layer robust optimization method in [15] is developed for multi-energy building. The upper layer optimizes the operating cost and user comfort, while the lower layer dispatches various distributed resources. In [17], a two-level energy management based on model predictive control (MPC) is designed to generate the optimal load decisions and track power references for residential microgrids. An MPC-based multi-time scale energy management model is presented in [18] to minimize the energy cost for a smart PV system with a consideration of the forecasting error. In [20], a stochastic hierarchical energy management for a home microgrid with PV, battery and flexible

Xin Lin and Gang Chen are with the School of Mechanical and Electrical Engineering, Sanming University, Sanming 365004, China (e-mail: xin.lin@fjsmu.edu.cn and chengang@fjsmu.edu.cn).

Ramon Zamora is with the Electrical and Electronic Engineering Department, Auckland University of Technology, Auckland 1142, New Zealand (e-mail: ramon.zamora@aut.ac.nz).

Yazhou Jiang is with the Electrical & Computer Engineering Department, Clarkson University, Potsdam, NY 13699 USA (e-mail: yjiang@clarkson.edu).

Anurag K. Srivastava is with the Computer Science and Electrical Engineering Department, West Virginia University, Morgantown, WV 26506-6695 USA (e-mail: anurag.srivastava@mail.wvu.edu).

loads is proposed to minimize the energy tariff and mitigate the impact of the PV uncertainties.

Research works in [15]–[21] can effectively reduce the energy bills. However, these studies only consider the low power density energy storage such as battery as an energy buffer, thereby increasing the power supply burden and shortening the cycle life of battery. Few works such as [22], [23] integrate supercapacitor (SC) into residential microgrids to compensate for high-frequency power to moderate the supply pressure of the battery, but these methods focus on the control design and ignore the economic benefits. Besides, the battery and SC degradation models are not completely considered. In [24] and [25] the multi-layer optimization methods are presented to minimize the operating cost. However, the proposed method only considers the SC component in the lower layer. This implies that the upper layer optimization will allocate more power to the battery and pass it to the lower-layer optimization as a reference, thereby increasing battery degradation cost. Furthermore, the proposed methods in [24] and [25] are not applied in the residential sector, thus failing to meet the user's comfort requirements. In addition, studies in [16]–[18], [20] concentrate on optimizing power usage and neglecting the user comforts. In [15], [19], the research works only integrate thermal comfort and ignore visual comfort. Very few studies such as [9], [11], [21], consider visual comfort. However, these works do not satisfy the users' requirement for visual comfort at different times. Moreover, the methods in [9], [11], [15], [19], [21] cannot reflect the consumer comfort level. In addition, the aforementioned methods focus on developing the optimization model but the interaction between control and optimization layers has not been fully discussed. Although a small number of HEMS, such as [26]–[28], consider local control systems, they fail to clarify the autonomous operation of system-level optimization in the event of a failure and plug-and-play (PnP) operation. In addition, these methods only consider battery systems.

According to the literature review, the shortcomings of the HEMS can be summarized as follows.

a. The economic benefits of a HEMS composed of battery and SC have not yet been thoroughly studied.
b. The current visual comfort models may not meet the user need at different times. In addition, the aforementioned methods cannot quantify the user comfort level.
c. The current HEMS only considers economic optimization method, without involving local control method. Besides, the interaction between optimization and control methods has not been fully discussed.

To address the issues above, this article proposes a multi-level HEMS for a DC household microgrid that integrates battery and SC. The proposed HEMS encompasses both the system-level and local-level HEMS. The main contributions are summarized as follows:

a. The system-level HEMS is an MPC-based multi-timescale optimization framework, which consists of long-term (LT) and short-term (ST) optimizations. The LT is to minimize the operating costs (including energy cost, battery and SC degradation costs) and to maximize user comforts (including visual and thermal comforts). The ST layer is to track the optimal cost scheduling provided by the LT layer to reduce cost error, suppress the power oscillations caused by the randomness of user behavior and PV generation, and ensure the feasible SoC level of the SC.
b. A visual comfort model is developed to meet the visual needs of occupants at different times. In addition, a discomfort model is designed to quantify the visual and thermal comfort ratings.
c. In the local-level HEMS, a droop-based coordinated control is presented to achieve power sharing between batteries and SCs, as well as DC bus voltage regulation without additional voltage control strategies. Besides, an advanced voltage regulator is proposed to achieve accurate power sharing and state of charge (SoC) balancing between batteries. Besides, the interaction between system- and local-level is fully studied.

The rest of this article is organized as follows. Section II presents the system configuration and model. Section III describes the system-level HEMS. Section IV presents the local-level HEMS. Simulation results are discussed in Section V. Finally, the conclusion and future trend is given in Section VI.

II. System Configuration and Model

A. System Configuration

The equivalent structure of the proposed HEMS is shown in Fig. 1. The HEMS consists of a PV generation, household appliances, battery-SC hybrid energy storage systems (HESS). Furthermore, the large-capacity battery and SC are replaced by multiple small-capacity batteries and SCs. The reason is that if one of the batteries or SCs fails, the other batteries or SCs can still continue to supply power, ensuring the stability of the bus voltage. It should be noted that the total capacity does not change. The appliance in the house consists of controllable, fixed and elastic loads. The controllable load indicates the load operation is regulated by HEMS, which includes lighting and thermal loads. The fixed load requires the based energy supply such as refrigerators. The elastic load, such as television, is mainly controlled by the stochastic behavior of the occupant.

In the initial stage, the system-level HEMS collects the relative data, such as real time price, weather conditions and forecasted hourly load profiles, etc. In system-level HEMS, the LT provides optimal decisions for household energy usage and user comfort based on the collected data. Then, the ST schedules power distribution based on the optimal decisions to

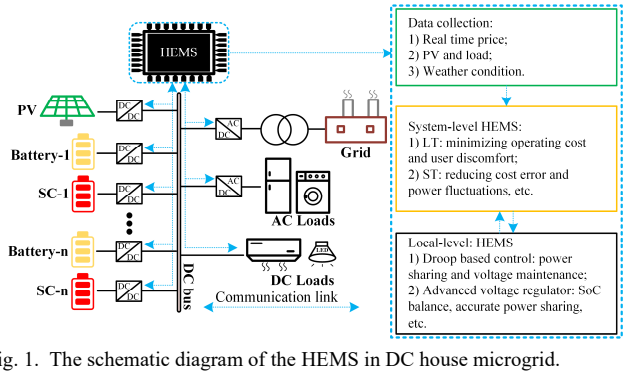

Fig. 1. The schematic diagram of the HEMS in DC house microgrid.

reduce cost errors, suppress power fluctuations generated by the random characteristics of PV and user behavior, and ensure the safety of the SoC of the SC. According to the power distribution scheme, the local-level HEMS determines the charging and discharging of the battery-SC systems, and the purchase/sale of the electricity from/to main grid. Furthermore, the local-level HEMS is capable of autonomously achieving power sharing, voltage and SoC regulation under conditions where the optimal power plan cannot be obtained from the system-level HEMS.

B. Modelling of Visual Discomfort

Visual comfort refers to the intensity of indoor light, which is usually expressed in illuminance. When the indoor illuminance is set by the user within a comfortable range, it will not cause discomfort. However, when the indoor illuminance is outside the set range, it will result in a discomfort effect. Generally, the indoor illuminance is produced by the lamps and the outdoor sunlight. The illuminance generated by lamps can be formulated as (1).

$$\phi_{\text{lamp}}(t) = \frac{P_{\text{lamp}}(t) \times \text{MF} \times \text{UF}}{A_t} \tag{1}$$

where $\phi_{\text{lamp}}(t)$ and $P_{\text{lamp}}(t)$ are the lighting illuminance and lighting power at time t. A_t, MF and UF are the total surface area, maintenance factor and utilization factor, respectively.

The illuminance produced by outdoor sunlight can be expressed as (2) and (3).

$$\phi_o(t) = (\alpha_o \times \varphi_s(t) + \beta_o) \times \text{DF} \tag{2}$$

$$\text{DF} = \frac{t_w \times c_w \times A_w \times \theta_v \times o_w}{A_t \times (1 - A_r^2)} \tag{3}$$

where $\phi_o(t)$ and $\varphi_s(t)$ are indoor illuminance generated by outdoor sunlight and global horizontal irradiance at time t. α_o and β_o are the measured parameters that can be obtained from [29]. Considering that β_o is small, hence, it is ignored in this article. DF, A_w and A_r are the daylight factor, window area and average reflectance. θ_v, t_w, c_w and o_w are the vertical angle of sky from the horizon, transmittance, correction and orientation factor for window. It should be considered that users have different visual comfort requirements at different times. During the daytime, users require higher visual illuminance to meet their daily work needs, while users need lower visual illuminance to satisfy their sleep demand at night time. Therefore, the indoor illuminance is written as (4) and (5).

$$\phi_{\text{in}}(t) = \begin{cases} \phi_{\text{lamp}}(t) + \phi_o(t), \text{ for } \phi_o(t) < \phi_d \\ 0, \qquad\qquad \text{for } \phi_o(t) \geq \phi_d \end{cases} \tag{4}$$

$$\phi_d = \begin{cases} \phi_d^{\text{nt}}, \text{ for } t \in [t_s^{\text{nt}}, t_e^{\text{nt}}] \\ \phi_d^{\text{rt}}, \text{ for } t \in [t_s^{\text{rt}}, t_e^{\text{rt}}] \\ 0, \quad \text{for } \phi_o(t) \geq \phi_d \end{cases} \tag{5}$$

where $\phi_{\text{in}}(t)$ and ϕ_d are indoor illuminance at time t and desired illuminance. ϕ_d^{dt} and ϕ_d^{nt} are the desired illuminance for day time and night time. t_s^{dt}, t_s^{nt}, t_e^{dt} and t_e^{nt} are the start and end of normal time and rest time. Equation (4) represents that $\phi_o(t)$ is less than ϕ_d, then the lamps will be involved in the regulation of the indoor illuminance. In contrast, when $\phi_o(t)$ is greater than and equal to ϕ_d, the lamps stop working.

The occupant's visual comfort is related to the indoor illuminance $\phi_{\text{in}}(t)$. To quantify visual comfort, an illuminance discomfort (IDC) index model is proposed, as shown in (6) and (7).

$$J_{\text{IDC}}(t) = 1 - (\alpha_{\text{IDC}} \times e^{\phi_{\text{IDC}}(t)} + \beta_{\text{IDC}}) \tag{6}$$

$$\phi_{\text{IDC}}(t) = \frac{|\phi_d - \phi_{\text{in}}(t)|}{\Delta\phi} \tag{7}$$

where $J_{\text{IDC}}(t)$ and $\Delta\phi$ are the IDC index cost function and deviation between the desired and marginal illuminance. $\phi_{\text{IDC}}(t)$, α_{IDC}, and β_{IDC} are the linking function and IDC factors. It can be observed from (6) and (7) that if $\phi_{\text{in}}(t)$ reaches the desired illuminance ϕ_d pre-specified by occupant, the IDC level for occupant is the lowest level that can be defined as 0. If $\phi_{\text{in}}(t)$ reaches the preset illuminance margin, it will cause the highest IDC to user, its value is defined as 1. By considering these two conditions, α_{IDC} and β_{IDC} are calculated as -0.5820 and 1.5820.

The visual comfort requires the reasonable assumptions, which can be summarized as follows:

- The indoor illuminance is evenly distributed inside the house, which can be considered as the average indoor illuminance.
- The lamps are engaged only when the room illuminance is below the pre-specified reference.
- At night time, the indoor illuminance is only provided by lamps, and the poor illuminance generated by moonlight is ignored.

C. Modelling of Thermal Discomfort

Thermal comfort refers to the occupant's satisfaction with the current thermal environment, which has a significant impact on the user's health. Low thermal comfort causes overcooling or overheating of the environment, which can lead to discomfort to customers. Based on the previous work in [30], a discrete thermal dynamic model is written as (8).

$$\begin{aligned} T_{\text{in}}(t+1) = T_{\text{in}}(t) \times \Bigg[1 - \frac{\Delta t}{c_{\text{in}}} \times \Big(\frac{1}{r_{\text{ir}}} + \frac{1}{r_{\text{ia}}} + \frac{1}{r_{\text{iw}}} + \frac{1}{r_{\text{im}}} + \frac{1}{r_{\text{dh}}}\Big)\Bigg] + \frac{\Delta t}{c_{\text{in}}} \\ \times \Bigg[\frac{T_r(t)}{r_{\text{ir}}} + \frac{T_w(t)}{r_{\text{iw}}} + \frac{T_m(t)}{r_{\text{im}}} + (1-\rho) \times A_w \times \varphi_s(t) \\ + \frac{T_a(t)}{r_{\text{ia}}} + \frac{T_{\text{dh}}(t)}{r_{\text{dh}}} + \delta \times P_{\text{CAC}}(t)\Bigg] \end{aligned} \tag{8}$$

where $T_{\text{in}}(t)$, $T_r(t)$, $T_w(t)$, $T_m(t)$, $T_a(t)$ and $T_{\text{dh}}(t)$ are the temperature of the indoor, house roof, exterior wall, inner wall, ambient and temperature caused by humidity. r_{ir}, r_{ia}, r_{iw}, r_{im} and r_{dh} are the thermal resistances in the house. c_{in} is the capacity of the indoor air. ρ and Δt are the proportion of the solar radiation acting on the inner wall and time interval. $P_{\text{CAC}}(t)$ is the output of the central air conditioning. δ is the switching factor, which is equal to -1 in summer and 1 in winter.

The customer's thermal comfort is directly regulated by the indoor temperature. If $T_{\text{in}}(t)$ satisfies the pre-defined temperature, the thermal discomfort of occupant reaches the lowest level. On the contrary, if $T_{\text{in}}(t)$ is far deviated from the setpoint temperature and reaches the boundary temperature, the thermal discomfort of occupant will be at the highest level. Then, a thermal discomfort (TDC) index model is proposed to quantify the thermal comfort, as shown in (9) and (10).

$$J_{\text{TDC}}(t) = 1 - (\alpha_{\text{TDC}} \times e^{T_{\text{TDC}}(t)} + \beta_{\text{TDC}}) \tag{9}$$

$$T_{\text{TDC}}(t) = \frac{|T_d - T_{\text{in}}(t)|}{\Delta T} \tag{10}$$

where T_d, $J_{\mathrm{TDC}}(t)$ and ΔT are the desired indoor temperature, TDC index cost function and deviation between the desired and marginal temperature. $T_{\mathrm{TDC}}(t)$, α_{TDC} and β_{TDC} are the linking function and TDC factors. Here, α_{TDC} and β_{TDC} are chosen to have the same value as in Section II-B.

D. Modelling of SC Degradation

SC is a high-power density energy storage with high lifetime and fast response characteristics. Therefore, SC is usually applied to provide transient power, thereby reducing the power supply burden of the battery. Since SC is also degraded during operation, HEMS needs to consider the degradation cost of SC to maximize the economic benefits of the operating cost in the house microgrid. In general, SC degradation is impacted by temperature and voltage [31]. The lifespan of the SC under extreme operating conditions such as under maximum temperature is greatly reduced. It can be assumed that the SC is operated at an ambient temperature in the house, so it can reach the pre-specified lifecycle provided by the manufacturer. In addition, the research work in [32] shows that the increase of charging and discharging current increases the aging rate of SC. This means that the SC power needs to be considered in the wearing model. Based on these conditions, the wear cost of energy per unit (kWh) for SC can be expressed as (11).

$$J_{\mathrm{sc}}(t) = \frac{\rho_{\mathrm{sc}}}{2\times\zeta_{\mathrm{sc}}\times Q_{\mathrm{sc}}} \tag{11}$$

where ρ_{sc}, Q_{sc}, $P_{\mathrm{sc}}(t)$ and ζ_{sc} are the price, capacity, power and total lifecycle of the SC, respectively. To calculate the total wear cost, equation (11) needs to be multiplied by the energy released or absorbed by SC, which can be written as (12).

$$J_{\mathrm{sc}}(t) = \frac{\rho_{\mathrm{sc}}}{2\times\zeta_{\mathrm{sc}}\times Q_{\mathrm{sc}}}\times P_{\mathrm{sc}}(t)\times\Delta t \tag{12}$$

where Δt is the time interval. It should be noted that the house is equipped with multiple SCs, and the SC capacity Q_{sc} can be further expressed as (13).

$$Q_{\mathrm{sc}} = \sum_{n=1}^{N} Q_{\mathrm{sc},\,n} \tag{13}$$

where $Q_{\mathrm{sc},\,n}$ is the capacity of the n^{th} SC. N is the total number of the SC.

E. Modelling of Battery Degradation

The battery degradation model reflects the degradation process during operation, which is directly related to the operating cost of HEMS. The total degradation cost model for battery during operation is written as (14).

$$J_b(t) = \frac{\rho_b}{Q_b\times\mathrm{DoD}_b(t)\times\zeta_b(t)\times\sqrt{\mu}}\times P_b(t)\times\Delta t \tag{14}$$

where $J_b(t)$, ρ_b and μ are the degradation cost, replacement cost and energy conversion efficiency. $P_b(t)$, Q_b, $\mathrm{DoD}_b(t)$ and $\zeta_b(t)$ are the battery output power, capacity, depth of discharge (DOD) and lifetime. The battery lifetime $\zeta_b(t)$ is a curve fitting function, which can be written as (15).

$$\zeta_b(t) = \alpha_b\times\mathrm{DoD}_b(t)^{-\beta_b}\times e^{-\gamma_b\times\mathrm{DoD}_b(t)} \tag{15}$$

where α_b, β_b and γ_b are the curve-fitting coefficients for lifetime function. $\mathrm{DoD}_b(t)$ is the ratio of the energy exported by the battery to its total capacity, as shown in (16).

$$\mathrm{DoD}_b(t) = \frac{P_b(t)\times\Delta t}{Q_b}. \tag{16}$$

Similar to SC, the house contains multiple battery units. Hence, the battery capacity Q_b can be presented as (17).

$$Q_b = \sum_{n=1}^{N} Q_{b,\,n} \tag{17}$$

where $Q_{b,\,n}$ is the capacity of the n^{th} battery.

F. Modelling of PV and Utility Cost

PV generation has the wear and tear during its operation, so HEMS should take into account the degradation cost of PV. The degradation cost of PV is the ratio between the investment cost and the service life, as shown in (18).

$$J_{\mathrm{PV}} = \frac{\rho_{\mathrm{PV}}}{24\times365\times n_{\mathrm{yr}}} \tag{18}$$

where J_{PV}, ρ_{PV} and n_{yr} are the PV hourly cost, investment cost and guaranteed years. It can be observed that (18) refers to the fixed degradation cost per hour of PV usage. The main grid electricity cost is written as (19) and (20).

$$J_g(t) = P_g(t)\times\delta_d\times\rho_{\mathrm{pr}}(t)\times\Delta t \tag{19}$$

$$\delta_d = \begin{cases}\delta_d^p, \text{ for } P_g(t)\geq 0\\ \delta_d^s, \text{ for } P_g(t) < 0\end{cases} \tag{20}$$

where $\eta_{\mathrm{pr}}(t)$ and $P_g(t)$ are the hourly electricity price and grid power at time t. δ_d is the discount rate. δ_d^p and δ_d^s are the purchase and sale discount rate.

G. Modelling of PV and Load Forecasting Error

Due to the randomness nature of PV generation and elastic load usage, the deviation may appear between hourly forecasting power and intra-hourly power usage. Then, a stochastic forecasting error is written as (21).

$$P_x^{\varepsilon}(t) = (1\pm\varepsilon)\times P_x^{\mathrm{hr}}(t) \tag{21}$$

where $P_x^{\varepsilon}(t)$ and $P_x^{\mathrm{hr}}(t)$ are the power with error and hourly power at time t. ε is error coefficient that is between 0 and 1. Specifically, x = LD denotes the load, while x = PV denotes the PV component.

III. Proposed System-Level HEMS

The system-level HEMS consists of MPC-based LT and ST optimization. LT is designed to minimize the operating cost, maintain user comfort and schedule power dispatch based on hourly forecasted data. ST layer is developed to track the optimal cost scheduling to reduce cost deviation, eliminate the power fluctuations, and maintain the feasible SoC level of the SC.

A. Modelling of Operation Constraints

The power balance constraint for LT and ST layers can be written as (22).

$$\begin{aligned}P_{\mathrm{LD}}(t) + P_{\mathrm{lamp}}(t) + P_{\mathrm{CAC}}(t)\\ = P_g(t) + P_{\mathrm{PV}}(t) + P_b(t) + P_{\mathrm{sc}}(t)\end{aligned} \tag{22}$$

where $P_{\mathrm{PV}}(t)$ and $P_{\mathrm{LD}}(t)$ are the PV power and load demand including fixed and elastic loads at time t.

The SoC variation models of the battery and SC can be expressed as (23) and (25).

$$\mathrm{SoC}_E(t+1) = \mathrm{SoC}_E(t) - \frac{\eta_E^c \times P_E(t) \times \Delta t}{Q_E}, \text{ for } P_E(t) \le 0 \quad (23)$$

$$\mathrm{SoC}_E(t+1) = \mathrm{SoC}_E(t) - \frac{P_E(t) \times \Delta t}{Q_E \times \eta_E^d}, \text{ for } P_E(t) > 0 \quad (24)$$

$$\mathrm{SoC}_E(t) = \frac{\sum_{n=1}^{N} \mathrm{SoC}_{E,n}(t)}{N} \quad (25)$$

where $\mathrm{SoC}_E(t)$ is the average SoC of energy storage, respectively. $\mathrm{SoC}_{E,n}(t)$ is the SoC of the n^{th} energy storage. η_E^c and η_E^d are the charging and discharging coefficients of energy storage. Specifically, $E = b$ denotes the battery, while E = SC denotes the SC component. The SoC and power constraints of the battery and SC can be written as (26) and (27).

$$\mathrm{SoC}_E^{\min} \le \mathrm{SoC}_E(t) \le \mathrm{SoC}_E^{\max} \quad (26)$$

$$P_E^{\min} \le P_E(t) \le P_E^{\max} \quad (27)$$

where $\mathrm{SoC}_E^{\min}$, $P_E^{\min}$, $\mathrm{SoC}_E^{\max}$ and $P_E^{\max}$ are the minimum and maximum SoC and power of the energy storage.

The power constraints of the grid, lighting and CAC are given in (28) – (30).

$$P_g^{\min} \le P_g(t) \le P_g^{\max} \quad (28)$$

$$P_{\text{lamp}}^{\min} \le P_{\text{lamp}}(t) \le P_{\text{lamp}}^{\max} \quad (29)$$

$$P_{\text{CAC}}^{\min} \le P_{\text{CAC}}(t) \le P_{\text{CAC}}^{\max} \quad (30)$$

where $P_g^{\min}$, $P_{\text{lamp}}^{\min}$, $P_{\text{CAC}}^{\min}$, $P_g^{\max}$, $P_{\text{lamp}}^{\max}$ and $P_{\text{CAC}}^{\max}$ are minimum and maximum power of the grid, lighting and CAC. The temperature and illuminance constraints are expressed by (31) and (32).

$$T_{\text{in}}^{\min} \le T_{\text{in}}(t) \le T_{\text{in}}^{\max} \quad (31)$$

$$\phi_{\text{in}}^{\min} \le \phi_{\text{in}}(t) \le \phi_{\text{in}}^{\max} \quad (32)$$

where $\phi_{\text{in}}^{\min}$, $T_{\text{in}}^{\min}$, $\phi_{\text{in}}^{\max}$ and $T_{\text{in}}^{\max}$ are the minimum and maximum illuminance and temperature.

Algorithm 1: MPC-based multi-timescale optimization

1. Load the dataset
2. Initialize system states
3. **For** $t_{\text{LT}} = 1{:}T_{\text{LT}}^{\text{opt}}$
4. Import data: $\left[P_{\text{LD}}(t_{\text{LT}}), P_{\text{PV}}(t_{\text{LT}}), \rho_{\text{pr}}(t_{\text{LT}}), \varphi_s(t_{\text{LT}}), T_a(t_{\text{LT}}), T_{\text{dh}}(t_{\text{LT}})\right]_{t_{\text{LT}}}^{t_{\text{LT}}+T_{\text{LT}}}$
5. Solve problem (33) – (35)
6. Obtain optimal control sequence and states: $\left[P_{\text{lamp}}^{\text{opt}}(t_{\text{LT}}), P_{\text{CAC}}^{\text{opt}}(t_{\text{LT}}), P_{\text{sc}}^{\text{opt}}(t_{\text{LT}}), P_b^{\text{opt}}(t_{\text{LT}}), P_g^{\text{opt}}(t_{\text{LT}})\right]_{t_{\text{LT}}}^{t_{\text{LT}}+T_{\text{LT}}}$ $\left[\mathrm{SoC}_b^{\text{opt}}(t_{\text{LT}}), \mathrm{SoC}_{\text{sc}}^{\text{opt}}(t_{\text{LT}}), \phi_{\text{in}}^{\text{opt}}(t_{\text{LT}}), T_{\text{in}}^{\text{opt}}(t_{\text{LT}})\right]_{t_{\text{LT}}}^{t_{\text{LT}}+T_{\text{LT}}}$
7. Apply first group control signal and states in the ST layer
8. **For** $t_{\text{ST}} = 1{:}T_{\text{ST}}^{\text{opt}}$
9. Import data and states: $\left[P_{\text{LD}}(t_{\text{ST}}), P_{\text{PV}}(t_{\text{ST}}), \rho_{\text{pr}}(t_{\text{ST}}), \varphi_s(t_{\text{ST}}), T_a(t_{\text{ST}}), T_{\text{dh}}(t_{\text{ST}})\right]_{t_{\text{ST}}}^{t_{\text{ST}}+T_{\text{ST}}}$ $\left[\mathrm{SoC}_b(t_{\text{ST}}), \mathrm{SoC}_{\text{sc}}(t_{\text{ST}}), \phi_{\text{in}}(t_{\text{ST}}), T_{\text{in}}(t_{\text{ST}})\right]_{t_{\text{ST}}}^{t_{\text{ST}}+T_{\text{ST}}}$
10. Solve problem (36) – (42)
11. Obtain optimal control sequence and states: $\left[P_{\text{lamp}}^{\text{opt}}(t_{\text{ST}}), P_{\text{CAC}}^{\text{opt}}(t_{\text{ST}}), P_{\text{sc}}^{\text{opt}}(t_{\text{ST}}), P_b^{\text{opt}}(t_{\text{ST}}), P_g^{\text{opt}}(t_{\text{ST}})\right]_{t_{\text{ST}}}^{t_{\text{ST}}+T_{\text{ST}}}$ $\left[\mathrm{SoC}_b^{\text{opt}}(t_{\text{ST}}), \mathrm{SoC}_{\text{sc}}^{\text{opt}}(t_{\text{ST}}), \phi_{\text{in}}^{\text{opt}}(t_{\text{ST}}), T_{\text{in}}^{\text{opt}}(t_{\text{ST}})\right]_{t_{\text{ST}}}^{t_{\text{ST}}+T_{\text{ST}}}$
12. Update first group optimal states in the step 9
13. Apply first group control signal in local-level HEMS
14. **End for**
15. Update optimal states in the LT layer: $\left[\mathrm{SoC}_b^{\text{opt}}(t_{\text{ST}}), \mathrm{SoC}_{\text{sc}}^{\text{opt}}(t_{\text{ST}}), \phi_{\text{in}}^{\text{opt}}(t_{\text{ST}}), T_{\text{in}}^{\text{opt}}(t_{\text{ST}})\right]_{t_{\text{ST}}=T_{\text{ST}}^{\text{opt}}}$
16. **End for**

Note: the superscript "opt" represents the optimal solution.

B. Formulation of Optimization Problem

The objective function of LT layer considering the indoor comfort and the degradation cost model of battery and SC is proposed to reduce the operating cost and maintain the occupant comfort. It can be expressed as (33) – (35).

$$\text{Min } J_{\text{LT}} = J_{\text{LT},1} + J_{\text{LT},2} \quad (33)$$

$$J_{\text{LT},1} = \sum_{t_{\text{LT}}=1}^{T_{\text{LT}}} [w_{\text{vis}} \times J_{\text{IDC}}(t_{\text{LT}}) + w_{\text{ther}} \times J_{\text{TDC}}(t_{\text{LT}})[\quad (34)$$

$$J_{\text{LT},2} = J_{\text{PV}} + \sum_{t_{\text{LT}}=1}^{T_{\text{LT}}} [w_{\text{sc}} \times J_{\text{sc}}(t_{\text{LT}}) + w_b \times J_b(t_{\text{LT}}) + w_g \times J_g(t_{\text{LT}})] \quad (35)$$

subject to the system models and constraints in (1) – (20) and (22) – (33). The control variables are $P_{\text{lamp}}(t_{\text{LT}})$, $P_{\text{CAC}}(t_{\text{LT}})$, $P_{\text{sc}}(t_{\text{LT}})$, $P_b(t_{\text{LT}})$ and $P_g(t_{\text{LT}})$. T_{LT} is the predictive horizon for LT optimization. w_{vis}, w_{ther}, w_{sc}, w_b and w_g are the weight coefficients. t_{LT} is the long-term index. It should be noted that the SC has low-capacity nature, its degradation cost still needs to be considered in LT layer. In addition, the output power of the SC indicates the average power in hourly load scheduling, it may frequently change within an hour.

The objective function of ST layer is written as (36) – (42).

$$\text{Min } J_{\text{ST}} = J_{\text{ST},1} + J_{\text{ST},2} + J_{\text{ST},3} + J_{\text{ST},4} + J_{\text{ST},5} \quad (36)$$

$$J_{\text{ST},1} = \sum_{t_{\text{ST}}=1}^{T_{\text{ST}}} \left[(P_{\text{lamp}}(t_{\text{LT}}) \times \Delta t_{\text{LT}} - P_{\text{lamp}}(t_{\text{ST}}) \times \Delta t_{\text{ST}}) \times \rho_{\text{pr}}(t_{\text{ST}}) \right]^2 \quad (37)$$

$$J_{\text{ST},2} = \sum_{t_{\text{ST}}=1}^{T_{\text{ST}}} \left[(P_{\text{CAC}}(t_{\text{LT}}) \times \Delta t_{\text{LT}} - P_{\text{CAC}}(t_{\text{ST}}) \times \Delta t_{\text{ST}}) \times \rho_{\text{pr}}(t_{\text{ST}}) \right]^2 \quad (38)$$

$$J_{\text{ST},3} = \sum_{t_{\text{ST}}=1}^{T_{\text{ST}}} \left[J_g(t_{\text{LT}}) - J_g(t_{\text{ST}}) \right]^2 \quad (39)$$

$$J_{\text{ST},4} = \sum_{t_{\text{ST}}=1}^{T_{\text{ST}}} [J_b(t_{\text{LT}}) - J_b(t_{\text{ST}})]^2 \quad (40)$$

$$J_{\text{ST},5} = \sum_{t_{\text{ST}}=1}^{T_{\text{ST}}} J_{\text{sc}}(t_{\text{ST}}) + \sum_{t_{\text{ST}}=T_{\text{ST}}}^{T_{\text{ST}}} [\mathrm{SoC}_{\text{sc}}^r - \mathrm{SoC}_{\text{sc}}(t_{\text{ST}})]^2 \quad (41)$$

$$T_{\text{ST}} = \frac{\Delta t_{\text{LT}}}{\Delta t_{\text{ST}}}. \quad (42)$$

subject to the system models and constraints in (1) – (32). t_{ST} is short-term index. Δt_{LT} and Δt_{ST} are long- and short-term interval. T_{ST} is the predictive horizon for LT optimization. $\mathrm{SoC}_{\text{sc}}^r$ and $\mathrm{SoC}_{\text{sc}}(t_{\text{ST}})$ are the SC's SoC reference and SoC level at time t_{ST}. Equations (37) – (40) indicates the minimization of the cost error between LT and ST layers. The second term of (41) is the SoC restoration method of the SC that is applied in the terminal time of the predictive horizon. Equation (42) is the relationship between the predictive horizon of the ST layer and time interval of the LT layer. Due to the nonlinear natures of the occupant discomfort and battery degradation models, the formulated problem in the LT and ST layers is a nonlinear programming that is addressed by the solver "FMINCON" in optimization tool box provided by MATLAB/Simulink.

The proposed MPC-based multi-timescale optimization is presented in Algorithm 1. The LT layer is to minimize the operating cost and occupant's discomfort, and deliver the optimal decisions to ST layer as references. Considering PV predicted error and load oscillation, the ST layer runs the optimization process and generate the optimal power variables. Then, the LT layer updates the states of the energy storage and indoor environment, and the optimization process enters the next time interval t_{LT}+1. The operating process is summarized as follow:

- It firstly defines the optimization horizon ($T_{\mathrm{LT}}^{\mathrm{opt}}$) and imports the data with a predicted horizon of T_{LT}.
- The objective function (33) – (35) in LT layer is solved to get the control sequence $\left[P_{\mathrm{lamp}}^{\mathrm{opt}}(t_{\mathrm{LT}}), P_{\mathrm{CAC}}^{\mathrm{opt}}(t_{\mathrm{LT}}), P_{\mathrm{sc}}^{\mathrm{opt}}(t_{\mathrm{LT}}), P_{b}^{\mathrm{opt}}(t_{\mathrm{LT}}), P_{g}^{\mathrm{opt}}(t_{\mathrm{LT}})\right]_{t_{\mathrm{LT}}}^{t_{\mathrm{LT}}+T_{\mathrm{LT}}}$ and system state sequence $\left[\mathrm{SoC}_{b}^{\mathrm{opt}}(t_{\mathrm{ST}}), \mathrm{SoC}_{\mathrm{sc}}^{\mathrm{opt}}(t_{\mathrm{ST}}), \phi_{\mathrm{in}}^{\mathrm{opt}}(t_{\mathrm{ST}}), T_{\mathrm{in}}^{\mathrm{opt}}(t_{\mathrm{ST}})\right]_{t_{\mathrm{ST}}}^{t_{\mathrm{ST}}+T_{\mathrm{ST}}}$. Only the control signal and system state of first time in sequence is selected as the reference value and initial states for the ST layer.
- The ST layer imports the data with the stochastic error at a predicted horizon T_{ST}. The function (36) – (42) will be solved to get the control sequence $\left[P_{\mathrm{lamp}}^{\mathrm{opt}}(t_{\mathrm{ST}}), P_{\mathrm{CAC}}^{\mathrm{opt}}(t_{\mathrm{ST}}), P_{\mathrm{sc}}^{\mathrm{opt}}(t_{\mathrm{ST}}), P_{b}^{\mathrm{opt}}(t_{\mathrm{ST}}), P_{g}^{\mathrm{opt}}(t_{\mathrm{ST}})\right]_{t_{\mathrm{ST}}}^{t_{\mathrm{ST}}+T_{\mathrm{ST}}}$ and state sequence $\left[\mathrm{SoC}_{b}^{\mathrm{opt}}(t_{\mathrm{ST}}), \mathrm{SoC}_{\mathrm{sc}}^{\mathrm{opt}}(t_{\mathrm{ST}}), \phi_{\mathrm{in}}^{\mathrm{opt}}(t_{\mathrm{ST}}), T_{\mathrm{in}}^{\mathrm{opt}}(t_{\mathrm{ST}})\right]_{t_{\mathrm{ST}}}^{t_{\mathrm{ST}}+T_{\mathrm{ST}}}$. The first set of control signals and states in the optimal sequence are selected to apply to the reference of the local-level HEMS and to update the states of the ST layers.
- The ST layer will complete the optimization task with time horizon $[t_{\mathrm{ST}}, t_{\mathrm{ST}} + T_{\mathrm{ST}}]$. The system state at the end time $T_{\mathrm{ST}}^{\mathrm{opt}}$ updates the system state of the LT layer. Then, the LT layer will move to the next time.

IV. Proposed Local-Level HEMS

The local-level HEMS regulates the power supply of the main grid, battery and SC according to the power reference signal from the system-level HEMS. In our previous work [33], a comprehensive control is proposed for DC microgrid. However, the proposed method does not show the interaction between control and optimization layers. In addition, the control parameters design of the consensus-based voltage regulator may have potential conflicts. By extending the work in [33], a coordinated droop control and advanced voltage regulator is proposed for battery and SC system in the local-level HEMS.

A. Modelling of Coordinated Droop Control

The coordinated droop control consists of *v-dP* and *v-P* droop methods, which can achieve power-sharing between battery and SC, maintain bus voltage without extra voltage recovery loop and restore SC voltage to the set point. A modified *v-dP* droop control is given in (43) – (44).

$$P_{b,n} = P_{b,n}^{\mathrm{ref}} + \frac{v_r - v_{b,n}}{k_b \times s} \tag{43}$$

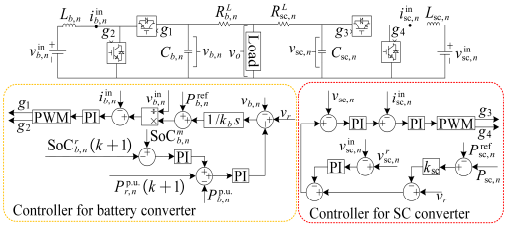

Fig. 2. The schematic diagram of the control circuit.

$$P_{b,n}^{\mathrm{ref}} = \frac{P_b(t_{\mathrm{ST}})}{N} \tag{44}$$

where k_b, v_r and $v_{b,n}$ are the droop coefficient, reference and output voltage of the n^{th} battery converter, ($n = 1, 2, \ldots, N$). $P_{b,n}$ is the output power of the battery converter. $P_{b,n}^{\mathrm{ref}}$ is the reference power. Equation (44) indicates that $P_b(t_{\mathrm{ST}})$ will be equally distributed among the number of N battery converters. A *v-P* control with SC voltage recovery is written as (45) -(47).

$$v_{\mathrm{sc},n} = v_r - k_{\mathrm{sc}} \times (P_{\mathrm{sc},n} - P_{\mathrm{sc},n}^{\mathrm{ref}}) - \delta v_{\mathrm{sc},n} \tag{45}$$

$$\delta v_{\mathrm{sc},n} = (k_{\mathrm{sc},n}^{p} + k_{\mathrm{sc},n}^{i}\frac{1}{s}) \times (v_{\mathrm{sc},n}^{r} - v_{\mathrm{sc},n}^{\mathrm{in}}) \tag{46}$$

$$P_{\mathrm{sc},n}^{\mathrm{ref}} = \frac{P_{\mathrm{sc}}(t_{\mathrm{ST}})}{N} \tag{47}$$

where k_{sc}, $v_{\mathrm{sc},n}$ and $P_{\mathrm{sc},n}$ are the droop coefficient, the output voltage and power of the n^{th} SC converter, respectively. $P_{\mathrm{sc},n}^{\mathrm{ref}}$ is the reference power. $\delta v_{\mathrm{sc},n}$ is the SC voltage recovery method. $v_{\mathrm{sc},n}^{r}$ and $v_{\mathrm{sc},n}^{\mathrm{in}}$ are the reference and measured voltage for the SC. $k_{\mathrm{sc},n}^{p}$ and $k_{\mathrm{sc},n}^{i}$ are the control parameters. Equation (47) means that $P_{\mathrm{sc}}(t_{\mathrm{ST}})$ will be equally distributed among the number of N SC converters. It should be noted the detail of bus voltage recovery method can be found in [33]. When the system- and local-level HEMS are operating normally, the voltage recovery control of SC stops working to avoid conflict with the SoC recovery in the system level HEMS.

B. Modelling of Advanced Voltage Regulator

The proposed advanced voltage regulator is defined by (48) – (50).

$$P_{b,n} = P_{b,n}^{\mathrm{ref}} + \frac{v_r - v_{b,n} + \delta v_n}{k_b \times s} \tag{48}$$

$$\delta v_n = \left[P_{r,n}^{\mathrm{p.u.}}(k+1) + \delta v_{\mathrm{SoC},n} - P_{b,n}^{\mathrm{p.u.}}\right] \times (k_{\mathrm{acc.},n}^{p} + k_{\mathrm{acc.},n}^{i}\frac{1}{s}) \tag{49}$$

$$\delta v_{\mathrm{SoC},n} = \left[\mathrm{SoC}_{b,n}^{m} - \mathrm{SoC}_{b,n}^{r}(k+1)\right] \times (k_{\mathrm{SoC},n}^{p} + k_{\mathrm{SoC},n}^{i}\frac{1}{s}) \tag{50}$$

where δv_n is the voltage compensation term. $\delta v_{\mathrm{SoC},n}$ is the SoC balance term. $P_{r,n}^{\mathrm{p.u.}}(k+1)$ and $P_{b,n}^{\mathrm{p.u.}}$ are the reference and output power in per unit for battery. $k_{\mathrm{acc.},n}^{p}$ and $k_{\mathrm{acc.},n}^{i}$ are the accurate power control parameters. $\mathrm{SoC}_{b,n}^{r}(k+1)$ and $\mathrm{SoC}_{b,n}^{m}$ are the average and measured SoC of the n^{th} battery. $k_{\mathrm{SoC},n}^{p}$ and $k_{\mathrm{SoC},n}^{i}$ are the SoC balance control parameters. Then, $P_{r,n}^{\mathrm{p.u.}}(k+1)$ and $\mathrm{SoC}_{b,n}^{r}(k+1)$ can be obtained by (51) – (53).

$$P_{r,n}^{\mathrm{p.u.}}(k+1) = P_{r,n}^{\mathrm{p.u.}}(0) + \varepsilon \sum_{j \in N_n} \delta_{\mathrm{acc.},nj}(k+1) \tag{51}$$

$$\delta_{\mathrm{acc.},nj}(k+1) = \delta_{\mathrm{acc.},nj}(k) + a_{\mathrm{acc.},nj}\left[P_{r,j}^{\mathrm{p.u.}}(k) - P_{r,n}^{\mathrm{p.u.}}(k)\right] \tag{52}$$

$$\mathrm{SoC}_{b,n}^{r}(k+1) = \mathrm{SoC}_{b,n}^{r}(0) + \varepsilon \sum_{j \in N_n} \delta_{\mathrm{SoC},nj}(k+1) \tag{53}$$

$$\delta_{\mathrm{SoC},nj}(k+1) = \delta_{\mathrm{SoC},nj}(k) + a_{\mathrm{SoC},nj}\left[\mathrm{SoC}_{b,j}^{r}(k) - \mathrm{SoC}_{b,n}^{r}(k)\right] \tag{54}$$

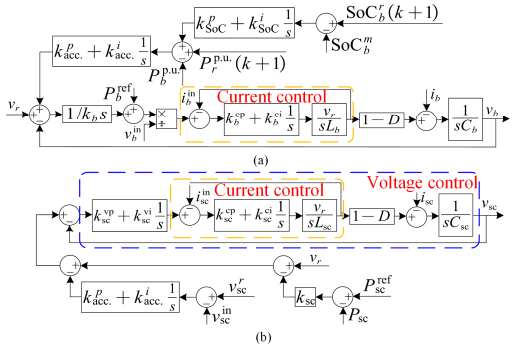

Fig. 3. The schematic diagram of the equivalent control circuit: (a) Battery converter control, and (b) SC converter control.

where $\mathrm{SoC}_{b,j}^{r}(0)$ is the initial SoC level. $P_{r,j}^{\mathrm{p.u.}}(0)$ is the initial output power of the battery converter. $\delta_{\mathrm{acc.},nj}(k)$ and $\delta_{\mathrm{SoC},nj}(k)$ are the variables that store the cumulative difference between agents n and j for power-sharing and SoC balance. $a_{\mathrm{acc.},nj}$ and $a_{\mathrm{SoC},nj}$ are the connection state between agents n and j for power-sharing and SoC balance. ε can adjust the convergence speed, which can be calculated by (55).

$$\varepsilon = \frac{2}{\beta_1(L) + \beta_{N-1}(L)} \tag{55}$$

where $\beta_n(\cdot)$ is the n^{th} largest eigenvalue of the symmetric matrix. L is the Laplacian matrix. Due to the small space of the house, communication delay is not considered.

The control principle is that if the average power in the accurate power sharing control is greater than the output power of the battery, the accurate power sharing control will generate a positive feedback voltage signal to increase the reference voltage value, so that the output power of the battery will increase. On the contrary, if the average power is less than the battery power, then the accurate power sharing method will send a negative feedback voltage signal to decrease the reference voltage of the control system, thereby reducing the output power of the battery. Therefore, accurate power sharing among batteries can be achieved. In the SoC balancing control, if the measured SoC is greater than average SoC obtained by the consensus algorithm, SoC balancing control then will send a positive power signal to increase the reference power in the accurate power-sharing control. Then the output of the battery is increased, and vice-versa. Hence, the SoC balance can be completed. The schematic diagram of the control circuit is shown in Fig. 2. The stability analysis of the control system is analyzed by root locus method. In addition, the control methods of the grid-connected mode and PV are traditional droop and power tracking controls.

C. System Stability Analysis

A common issue is that the control system might experience potential stability degradation due to the interaction between interconnected converters. Therefore, the control parameters need to be meticulously designed to ensure the stable operation of the system. In the proposed method, the SC converter uses the outer voltage and inner current control loops, while the battery converter only employs constant current control. The schematic diagram of the equivalent control circuit for the battery and SC is shown in Fig. 3. The control parameters can be calculated by using (56) based on [34].

$$\begin{aligned} k_x^{\mathrm{vp}} &= \frac{\omega_{x,v} C_x}{1-D} \quad k_x^{\mathrm{cp}} = \frac{\omega_{x,c} L_x}{v_r} \\ k_x^{\mathrm{vi}} &= \frac{\eta \omega_{x,v}^2 C_x}{1-D} \quad k_x^{\mathrm{ci}} = \frac{\eta \omega_{x,c}^2 L_x}{v_r} \end{aligned} \tag{56}$$

where k_x^{vp}, k_x^{cp}, k_x^{vi}, and k_x^{ci} are the proportional and integral parameters for the voltage and current control loop, respectively. It should be noted that $x = b$ presents the battery, and $x = \mathrm{sc}$ denotes the SC component. $\omega_{x,v}$ and $\omega_{x,c}$ are the control bandwidth of the voltage and current loops. η and D are the proportional coefficient and steady state value of the duty cycle. L_x and C_x are the filter inductor and filter capacitor, respectively. It is worthy noted that the dynamic response of the SC is much faster than the response speed of the battery. Therefore, the current control bandwidth of the battery is smaller than the bandwidths of the SC.

According to Fig. 3, the small signal model of the output impedance of the SC converter can be obtained from (57).

$$z_{\mathrm{sc}} = -\frac{\hat{v}_{\mathrm{sc}}}{\hat{i}_{\mathrm{sc}}} = \frac{b_{12}s^2 + b_{11}s + b_{10}}{a_{13}s^3 + a_{12}s^2 + a_{11}s + a_{10}} \tag{57}$$

where $a_{13} = C_{\mathrm{sc}}$; $a_{12} = k_{\mathrm{sc}}^{\mathrm{vp}}(1-D)[1 - k_{\mathrm{sc}}^{p}(1-D)]$; $a_{11} = k_{\mathrm{sc}}^{\mathrm{vi}}(1-D) - (k_{\mathrm{sc}}^{i}k_{\mathrm{sc}}^{\mathrm{vp}} + k_{\mathrm{sc}}^{p}k_{\mathrm{sc}}^{\mathrm{vi}})(1-D)^2$; $a_{10} = -k_{\mathrm{sc}}^{\mathrm{vi}}k_{\mathrm{sc}}^{i}(1-D)^2$; $b_{12} = k_{\mathrm{sc}}k_{\mathrm{sc}}^{\mathrm{vp}}v_{\mathrm{sc}}^{\mathrm{in}} + 1$; $b_{11} = k_{\mathrm{sc}}k_{\mathrm{sc}}^{\mathrm{vi}}v_{\mathrm{sc}}^{\mathrm{in}}$; $b_{10} = 0$.

Similarly, the small-signal model of the output impedance of the battery converter is given by (58).

$$\begin{aligned} z_b &= -\frac{\hat{v}_b}{\hat{i}_b} \\ &= \frac{b_{26}s^6 + b_{25}s^5 + b_{24}s^4 + b_{23}s^3 + b_{22}s^2 + b_{21}s + b_{20}}{a_{27}s^7 + a_{26}s^6 + a_{25}s^5 + a_{24}s^4 + a_{23}s^3 + a_{22}s^2 + a_{21}s + a_{20}} \end{aligned} \tag{58}$$

where $a_{27} = L_bQ_bRC_bk_bP_{\max}(v_b^{\mathrm{in}})^2$; $a_{26} = Q_bRC_bk_bk_b^{\mathrm{cp}}P_{\max}(v_b^{\mathrm{in}})^2v_r$; $a_{25} = Q_bRC_bk_bk_b^{\mathrm{ci}}P_{\max}(v_b^{\mathrm{in}})^2v_r$; $a_{24} = Q_b(1-D)k_b^{\mathrm{cp}}v_b^{\mathrm{in}}(RP_{\max}v_r - 2k_{\mathrm{acc.}}^{p}v_r^2)$; $a_{23} = (1-D)[2k_{\mathrm{acc.}}^{p}v_r^2(k_b^{\mathrm{cp}}k_{\mathrm{SoC}}^{p}P_{\max} - Q_bk_b^{\mathrm{ci}}v_b^{\mathrm{in}}) - Q_bP_{\max}v_b^{\mathrm{in}}(2k_{\mathrm{acc.}}^{i}k_b^{\mathrm{cp}}v_r^2 - Rk_b^{\mathrm{ci}}v_r)]$; $a_{22} = 2(1-D)v_r^2(k_{\mathrm{acc.}}^{i}k_b^{\mathrm{cp}}k_{\mathrm{SoC}}^{p}P_{\max} - Q_bk_{\mathrm{acc.}}^{i}k_b^{\mathrm{ci}}v_b^{\mathrm{in}} + Q_bk_{\mathrm{acc.}}^{p}k_b^{\mathrm{ci}}k_{\mathrm{SoC}}^{p}P_{\max} + Q_bk_{\mathrm{acc.}}^{p}k_b^{\mathrm{cp}}k_{\mathrm{SoC}}^{i}P_{\max})$; $a_{21} = 2(1-D)P_{\max}v_r^2[k_{\mathrm{acc.}}^{i}(k_b^{\mathrm{ci}}k_{\mathrm{SoC}}^{p} + k_b^{\mathrm{cp}}k_{\mathrm{SoC}}^{i}) + k_{\mathrm{acc.}}^{p}k_b^{\mathrm{ci}}k_{\mathrm{SoC}}^{i}]$; $a_{20} = 2(1-D)k_{\mathrm{acc.}}^{i}P_{\max}v_r^2k_b^{\mathrm{ci}}k_{\mathrm{SoC}}^{i}$; $b_{26} = L_bQ_bRk_bP_{\max}(v_b^{\mathrm{in}})^2$; $b_{25} = Q_bRk_bk_b^{\mathrm{cp}}P_{\max}(v_b^{\mathrm{in}})^2v_r$; $b_{24} = Q_bRk_bk_b^{\mathrm{ci}}P_{\max}(v_b^{\mathrm{in}})^2v_r$; $b_{23} = b_{22} = b_{21} = b_{20} = 0$.

The total output impedance can be written as (59).

$$z_o = \frac{z_{\mathrm{sc}}z_b}{z_{\mathrm{sc}} + z_b} \tag{59}$$

Then, substituting (57) and (58) into (59), the characteristics function of the control system is given as (60).

$$a_8s^8 + a_7s^7 + a_6s^6 + a_5s^5 + a_4s^4 + a_3s^3 + a_2s^2 + a_1s + a_0 = 0 \tag{60}$$

where $a_8 = L_bQ_bRP_{\max}k_b(v_b^{\mathrm{in}})^2[C_b(1 + k_{\mathrm{sc}}k_{\mathrm{sc}}^{\mathrm{vp}}v_{\mathrm{sc}}^{\mathrm{in}}) + C_{\mathrm{sc}}]$;

$a_7 = Q_bRP_{\max}(v_b^{\mathrm{in}})^2k_b\{C_bk_b^{\mathrm{cp}}v_r(1 + k_{\mathrm{sc}}k_{\mathrm{sc}}^{\mathrm{vp}}v_{\mathrm{sc}}^{\mathrm{in}}) + L_b(1-D)k_{\mathrm{sc}}^{\mathrm{vp}}[1 - (1-D)k_{\mathrm{sc}}^{p}] + C_{\mathrm{sc}}k_b^{\mathrm{cp}}v_r + L_bC_bk_{\mathrm{sc}}k_{\mathrm{sc}}^{\mathrm{vi}}v_{\mathrm{sc}}^{\mathrm{in}}\}$;

$a_6 = Q_bR(v_b^{\mathrm{in}})^2k_bP_{\max}\{k_b^{\mathrm{ci}}v_r(C_b + C_{\mathrm{sc}}) + (1-D)(k_b^{\mathrm{cp}}k_{\mathrm{sc}}^{\mathrm{vp}}v_r + L_bk_bk_{\mathrm{sc}}^{i}) - (1-D)^2[(L_b(k_{\mathrm{sc}}^{i}k_{\mathrm{sc}}^{\mathrm{vp}} + k_{\mathrm{sc}}^{p}k_{\mathrm{sc}}^{\mathrm{vi}}) + k_b^{\mathrm{cp}}k_{\mathrm{sc}}^{p}k_{\mathrm{sc}}^{\mathrm{vp}}v_r)] + C_bk_{\mathrm{sc}}v_rv_{\mathrm{sc}}^{\mathrm{in}}(k_b^{\mathrm{ci}}k_{\mathrm{sc}}^{\mathrm{vp}} + k_b^{\mathrm{cp}}k_{\mathrm{sc}}^{\mathrm{vi}})\}$;

$a_5 = Q_b(1-D)v_b^{\mathrm{in}}v_r[Rk_b^{\mathrm{cp}}P_{\max}(1 + k_bk_{\mathrm{sc}}^{\mathrm{vi}}v_b^{\mathrm{in}} + k_{\mathrm{sc}}k_{\mathrm{sc}}^{\mathrm{vp}}v_{\mathrm{sc}}^{\mathrm{in}}) - 2k_b^{\mathrm{cp}}$

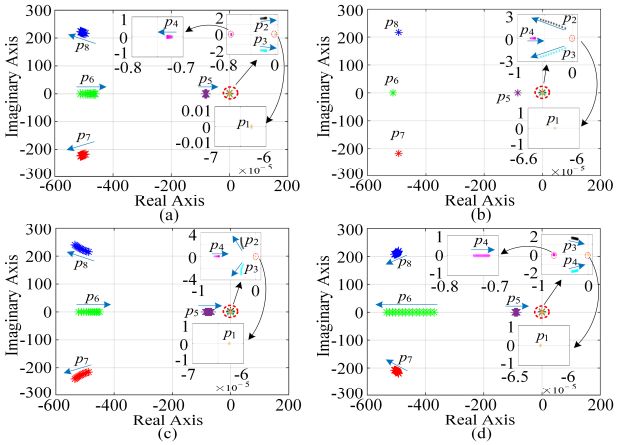

Fig. 4. Root locus diagram: (a) k_{sc} is between 0.0015 and 0.01 V/W, while k_b is between 0 and 0.008 V/W, (b) k^p_{SoC} is between 1 and 5, while k^i_{SoC} is between 0.0006 and 0.0031, (c) $k^p_{acc.}$ is between 10 and 100, while $k^i_{acc.}$ is between 6.2832 and 62.832, and (d) $k^p_{sc.}$ is between 0.03 and 0.3, while $k^i_{acc.}$ is between 0.00018 and 0.0018.

$$k^p_{acc.}(v_r + k_{sc}k^{vp}_{sc}P_{max}v^{in}_b v^{in}_{sc}) + Rk_b k^{ci}_b k^{vp}_{sc}P_{max}v^{in}_b] - Q_b(v^{in}_b)^2 P_{max}$$

$$Rk_b\{(1-D)^2[k^{vi}_{sc}(L_b k^i_{sc} + k^{cp}_b k^p_{sc}v_r) + k^{vp}_{sc}v_r(k^{ci}_b k^p_{sc} + k^{cp}_b k^i_{sc})] + C_b k^{ci}_b k_{sc}k^{vi}_{sc}v_r v^{in}_{sc}\};$$

$$a_4 = (1-D)\{2k^p_{acc.}k^{cp}_b P_{max}v_r^2 - Q_b v^{in}_b v_r[2(k^i_{acc.}k^{cp}_b + k^p_{acc.}k^{ci}_b v_r) - Rk^{ci}_b P_{max}(1 + k_b k^{vi}_{sc}v^{in}_b)] - 2Q_b k_{sc}v_r^2 v^{in}_{sc}[k^p_{acc.}v^{in}_b(k^{ci}_b k^{vp}_{sc} + k^{cp}_b k^{vi}_{sc}) + k^{cp}_b k^{vp}_{sc}(k^i_{acc.}v^{in}_b - k^p_{acc.}k^p_{SoC}P_{max})] + Q_b RP_{max}v^{in}_b v_r v^{in}_{sc}k_{sc}(k^{ci}_b k^{vp}_{sc} + k^{cp}_b k^{vi}_{sc})\} - (1-D)^2 Q_b Rk_b P_{max}(v^{in}_b)^2 v_r(k^{ci}_b k^i_{sc}k^{vp}_{sc} + k^{ci}_b k^p_{sc}k^{vi}_{sc} + k^{cp}_b k^i_{sc}k^{vi}_{sc});$$

$$a_3 = Q_b(1-D)\{2P_{max}v_r^2 k^p_{acc.}(k^{ci}_b k^p_{SoC} + k^{cp}_b k^i_{SoC})(1 + k_{sc}k^{vp}_{sc}v^{in}_{sc}) + 2P_{max}v_r^2 k^{cp}_b k_{sc}v^{in}_{sc}(k^i_{acc.}k^{vp}_{sc}k^p_{SoC} + k^p_{acc.}k^{vi}_{sc}k^p_{SoC} + k^p_{acc.}k^{vp}_{sc}k^i_{SoC}) - k_{sc}v^{in}_b v_r^2 v^{in}_{sc}(k^i_{acc.}k^{ci}_b k^{vp}_{sc} + k^i_{acc.}k^{cp}_b k^{vi}_{sc} + k^p_{acc.}k^{ci}_b k^{vi}_{sc}) - k^{ci}_b v^{in}_b v_r[2k^i_{acc.}v_r + R(1-D)k_b k^i_{sc}k^{vi}_{sc}P_{max}v^{in}_b - Rk_{sc}k^{vi}_{sc}P_{max}v^{in}_{sc}]\};$$

$$a_2 = 2(1-D)v_r^2[P_{max}k^i_{SoC}(k^i_{acc.}k^{cp}_b + k^p_{acc.}k^{ci}_b) + k^i_{acc.}k^{cp}_b k_{sc}P_{max}v^{in}_{sc}(k^{vi}_{sc}k^p_{SoC} + k^{vp}_{sc}k^i_{SoC} + k^{vi}_{sc}k^i_{SoC}) + k^p_{acc.}k^{ci}_b k_{sc}P_{max}v^{in}_{sc}(k^{vi}_{sc}k^p_{SoC} + k^{vp}_{sc}k^i_{SoC}) + k^i_{acc.}k^{ci}_b(P_{max}k^p_{SoC} - Q_b k_{sc}k^{vi}_{sc}v^{in}_b v^{in}_{sc} + P_{max}k_{sc}k^{vp}_{sc}k^p_{SoC})];$$

$$a_1 = 2(1-D)k^{ci}_b P_{max}v_r^2[k^i_{SoC}(k^i_{acc.} + k^p_{acc.}k_{sc}k^{vi}_{sc}v^{in}_{sc}) + k^i_{acc.}k_{sc}v^{in}_{sc}(k^{vi}_{sc}k^p_{SoC} + k^{vp}_{sc}k^i_{SoC} + k^{vi}_{sc}k^i_{SoC})];$$

$$a_0 = 2(1-D)k^i_{acc.}k^{ci}_b k_{sc}k^{vi}_{sc}k^i_{SoC}P_{max}v_r^2 v^{in}_{sc}.$$

According to (58), the analysis of system stability can be conducted by observing the location of the dominant pole in the root locus plot. Subsequently, control parameters should be suitably selected to guarantee the controller's performance and the system's safe operation. From Fig. 4(a), it can be observed that there are eight eigenvalues. Among them, three eigenvalues (p_6, p_7, and p_8) are far from the right half of the S-plane and therefore do not play a dominant role. As k_{sc} and k_b vary within the specified range, p_1 is located on the left half of the S-plane. This means that the stability of the control system can be ensured. Furthermore, p_4 moves to the left side. This indicates that the stability of the system gradually improves. Although p_2, p_3, and p_5 all move forward to the left, they are still within the left half-plane. Therefore, the control system can continuously operate stably. Similarly, as can be seen from Fig. 4(b) to 4(d), with the change of control parameters, the main eigenvalues are located on the left side of the S-plane, thereby eliminating the instability of the control system.

V. Simulation Results

A. Simulation Setup

To verify the performance of the proposed model, the processor in the loop (PIL) simulation platform including a host PC and microcontroller (MC), is established, as illustrated in the Fig. 5. The system-level HEMS operates on the host PC to generate the optimal power scheduling plan. The plan is sent to the system-level HEMS installed in the MC through a communication link. Subsequently, the MC transmits control signals to adjust the power output of the controlled target. Finally, the system-level HEMS will update the system status. The model of the MC is STM32F429ZIT6. Then, the HEMS environment includes the summer and winter days. The public datasets including hourly electricity tariff, weather, fixed and elastic loads are obtained from National Renewable Energy Lab and Ameren Illinois Power Company to verify the proposed method [35], [36]. The equivalent structure of the house DC microgrid is shown in Fig. 1, which contains a PV generation,

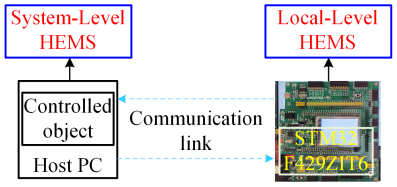

Fig. 5. The PIL simulation platform.

TABLE I [4], [11], [20], [24]
PARAMETERS FOR MULTI-LEVEL HEMS

Parameters settings for visual comfort					
P^{max}_{lamp}	P^{min}_{lamp}	MF	UF	A_t	α_o
1.2 kW	0 kW	0.9	0.9	268 m^2	110
t_w	c_w	A_w	θ_v	o_w	A_r
0.9	0.5	5 m^2	90°	1	0.3
Parameters settings for thermal comfort					
P^{max}_{CAC}	P^{min}_{CAC}	r_{ir}	r_{ia}	r_{iw}	r_{im}
5 kW	0 kW	8.557 °C/kW	99.106 °C/kW	98.940 °C/kW	52.263 °C/kW
r_{dh}	c_{in}	ρ	-	-	-
98.378 °C/kW	9.984 kWh/°C	0.6	-	-	-
Parameters settings for battery degradation					
ρ_b	Q_b	μ	P^{max}_b	P^{min}_b	SoC^{max}_b
600 $	12 kWh	0.98	4 kW	-4 kW	90 %
SoC^{min}_b	α_b	β_b	γ_b	η^c_b, η^d_b	-
10 %	4980	1.98	0.016	0.98	-
Parameters settings for SC degradation					
ρ_{sc}	ζ_{sc}	Q_{sc}	P^{max}_{sc}	P^{min}_{sc}	SoC^{max}_{sc}
2400 $	50000	3 kWh	10 kW	-10 kW	90 %
SoC^{min}_{sc}	η^c_{sc}, η^d_{sc}	-	-	-	-
10 %	0.98	-	-	-	-
Parameters settings for grid and PV					
P^{max}_g	P^{min}_g	ρ_{PV}	n_{yr}	-	-
5 kW	-5 kW	6220 $	25	-	-
Parameters settings for controls and DC/DC converters					
v^{in}_b, v^{in}_{sc}	C_b, C_{sc}	L_b, L_{sc}	k_b	k_{sc}	k^p_{sc}
150 V	200 μF	3 mH	0.0016 V/W	0.01 V/W	0.1
k^i_{sc}	v^r_{sc}	$k^p_{acc.}$	$k^i_{acc.}$	k^p_{SoC}	k^i_{SoC}
0.0016	75 V	50	31.4159	3	0.0002
$R^L_{b,1}$, $R^L_{sc,1}$	$R^L_{b,2}$, $R^L_{sc,2}$	$R^L_{b,2}$, $R^L_{sc,2}$	v_r	k^{vp}_{sc}	k^{vi}_{sc}
0.01 Ω	0.02 Ω	0.03 Ω	220 V	0.3949	24.8150
k^{cp}_{sc}	k^{ci}_{sc}	k^{cp}_b	k^{ci}_b	-	-
0.0286	17.9447	0.0143	4.4862	-	-

three batteries, three SCs, and house loads. The desired indoor illuminances are set to 0.3 klx and 0.0025 klx at 6:00-22:00 and 22:00-6:00, respectively. The illuminance deviations are ±0.02 klx and ±0.0025 klx at 6:00-22:00 and 22:00-6:00, respectively. The desired indoor temperatures are 23 ℃ and 22 ℃ in summer and winter, respectively. The temperature error is ±2 ℃. The discount rates for purchasing and selling electricity between HEMS and the grid are set at 1 and 0.8. The long- and short-term intervals are 1 h and 5 min. The total optimization horizons for LT and ST layers are 24 h and 60 min. The default predictive horizons for LT and ST layers are set to 12 h and 60 min, respectively. The system parameters are given in Table I. The cases in Section V-B to V-D are executed in MATLAB, while studies in Section V-E and V-F are run in Simulink.

B. Power Scheduling and Operating Cost

This case studies the power scheduling and operating cost under different forecasting error conditions. The forecasting errors are generated by uncertainties to indicate the power mismatch between hourly power scheduling and intra-hourly power usage. This means that intra-hourly power consumption may be higher or lower than hourly power scheduling. The error rates are 0%, 20%, 40 % and 60 %. The winter datasets are employed in this case.

As can be seen from Fig. 6(a), the lowest electricity price of the day occurs between 0:00-7:00. The electricity price fluctuates around $0.14 per kWh from 7:00 to16:00. The electricity price gradually increases and reaches its peak between 16:00-19:00. Subsequently, the electricity price begins to decline but experiences a brief rebound at 21:00, eventually dropping to its lowest point. From Fig. 6(b), the PV system is unable to generate electricity due to insufficient solar irradiance between 0:00 and 11:00. The PV power generation gradually

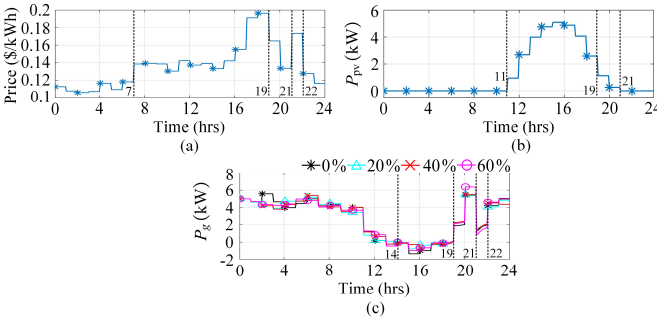

Fig. 6. Power scheduling: (a) Real-time price, (b) PV power generation, and (c) Grid power scheduling under different forecasting error rates.

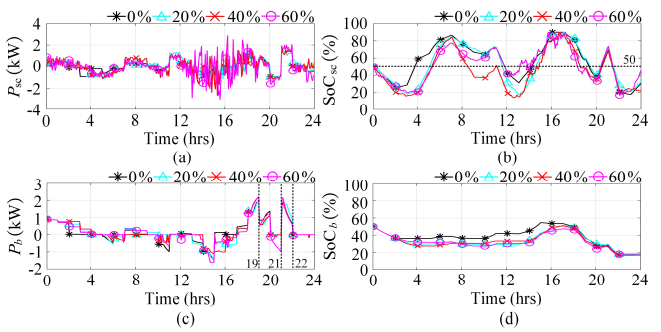

Fig. 7. HESS power scheduling under different forecasting error rates: (a) The output power of the SC, (b) The SoC variations of the SC, (c) The output power of the battery, and (d) The SoC variations of the battery.

TABLE II
OPERATING COST IN DIFFERENT ERRORS

	Proposed Method			
	ε = 0 %	ε = 20 %	ε = 40 %	ε = 60 %
LT-O ($)	8.3795	8.4425	8.5196	8.6218
LT-B ($)	0.2377	0.2437	0.2750	0.3024
LT-SC ($)	0.0295	0.0307	0.0335	0.0316
ST-O ($)	8.4222	8.4945	8.5814	8.6949
ST-B ($)	0.2046	0.2449	0.2438	0.2674
ST-SC ($)	0.0260	0.0303	0.0346	0.0414
Δ-LT-ST ($)	0.0427	0.0520	0.0618	0.0731
	Method-I			
	ε = 0 %	ε = 20 %	ε = 40 %	ε = 60 %
LT-O ($)	8.7607	8.8518	8.8715	8.8905
LT-B ($)	0.4434	0.5383	0.4271	0.4389
ST-O ($)	8.6337	8.7375	8.7854	8.8180
ST-B ($)	0.3000	0.3926	0.2830	0.2998
ST-SC ($)	0.0032	0.0111	0.0185	0.0271
Δ-LT-ST ($)	0.1270	0.1143	0.0861	0.0725
	Method-II			
	ε = 0 %	ε = 20 %	ε = 40 %	ε = 60 %
LT-O ($)	9.0842	9.2163	9.2916	9.2363
LT-B ($)	1.0693	1.0314	1.0763	0.9769
ST-O ($)	8.7440	8.9201	9.0587	9.0641
ST-B ($)	0.6254	0.6378	0.6789	0.6681
Δ-LT-ST ($)	0.3402	0.2962	0.2329	0.1722
	Method-III			
	ε = 0 %	ε = 20 %	ε = 40 %	ε = 60 %
LT-O ($)	13.4557	13.4387	13.4373	13.4440
ST-O ($)	13.4557	13.4414	13.4360	13.4169

Note: O is the operating cost; B is the battery cost; SC is the supercapacitor cost; Δ-LT-ST is the cost error between the LT and ST layers.

increases and reaches its peak from 11:00 to 16:00, subsequently declining slowly until it reaches lowest point at 21:00. As observed from Fig. 6(c), the grid power does not exhibit high-frequency power fluctuations at different error rates. In detail, the utility delivers power to the home microgrid at beginning due to lower power price. Then, the HEMS sells electricity to the utility during 14:00 and 19:00 due to higher electricity price and PV generation. Both real-time tariff and PV generation decrease during 19:00 and 21:00. The HEMS will purchase more power from the main grid. Then, the power from the utility drops during 21:00 and 22:00 since the electricity tariff suddenly rises. Subsequently, the electricity price decreased, and the HEMS purchases more electricity from the utility.

From Fig. 7(a), the SC power shows high frequency fluctuations under different error conditions. This is because the SC provides the transient power to compensate for the power deviation between hourly load scheduling and intra-hourly power usage. From Fig. 7(b), the SoC of the SC varies around the setpoint that is 50 %. This indicates that the SoC recovery of the SC in HEMS can avoid the SoC of the SC being in the high or low SoC state. Unlike SC component, the power and SoC of the battery does not show frequent variations under different error conditions, as shown in Figs. 7(c) and 7(d). This indicates that the battery only provides average power in the HEMS. Furthermore, due to the increase in electricity prices from 16:00 to 19:00, the HEMS halts purchasing electricity from the main grid, resulting in a gradual rise in the output power of the battery until it reaches maximum value, as shown in Fig. 6(a), Fig. 6(c) and Fig. 7(c). Subsequently, the output power of the battery gradually decreased, but suddenly increased at 21:00. This is due to a temporary rise in electricity

TABLE III
COST AND COMPUTATION TIME FOR DIFFERENT PREDICTIVE HORIZONS

Horizon (h)	6	12	18	24	30
LT-O ($)	8.4590	8.3795	8.6547	8.5843	8.6374
ST-O ($)	8.5640	8.4222	8.6924	8.6187	8.6588
LT-CT (s)	0.6266	1.7802	3.4456	6.3999	11.7980
ST-CT (s)	0.7869	1.1299	0.7448	0.7563	0.7221

Note: CT is the computation time.

prices during this time, leading to a decrease in power supply from the main grid. In summary, the HEMS can formulate efficient utility and HESS power plans based on real-time price, PV generation variations and different error rates.

The operating cost of the proposed method is compared with other methods that include method-I, method-II and method-III. Method-I in [24], [25] indicates only ST layer considers the SC component. Method-II only uses the battery as an energy buffer and they are common approach in literature review. Method-III presents that the HEMS only considers occupant comfort without including PV and ESS. The results are given in Table II. It should be noted that the LT layer generates the expected operating costs. Then, the operating cost in the ST layer can be considered as the actual cost due to the short time interval.

From Table II, the operating cost error between the LT and ST layers in the proposed method is small under different errors. They are 0.0427, 0.0520, 0.0618 and 0.0731, respectively. This means that the ST layer in the proposed method can track the operating cost scheduling provided by the LT layer. In addition, the microgrid operating cost and the degradation cost of the battery and SC will increase with the change of errors. The operating cost of the LT and ST layers in Method-I are higher than the proposed method. The reason for this is that the power scheduling generated by the LT layer in Method-I only considers the battery as energy buffer. As a result, the battery degradation cost of the LT layer in Method-I is significantly more than the proposed method. In addition, the ST layer in Method-I is designed to track the power scheduling of the LT layer. This also results in the SC component supplying a small amount of power to the system. As observed from Table II, the degradation cost of SC is almost negligible compared to the operating cost of the system. This is why the degradation cost of SC and reduction of the operating cost in the proposed method is higher than Method-I. This refers to the fact that the SC in the proposed method can participate in the operation of the system more frequently. In addition, the operating cost in Method-II and Method-III is significantly greater than that of the proposed method. Therefore, the proposed method is superior to Method-I, Method-II and Method-III.

Table III shows the operating costs at different predictive horizons. The operating cost in the predictive horizon of 6 h is higher than the one in the predictive horizon of 12 h. The costs do not vary significantly over the predictive range of 18-30 h. This shows that the system operating cost will not always decrease with the increase of the predictive horizon. Therefore, the predictive horizon is chosen as 12 h in this article. In addition, as the predictive horizon increases, the computation time of the LT layer will obviously increase. Nevertheless, the calculation time is much smaller than the time interval (1 h) of the LT layer. Similarly, the calculation time of the ST layer is also much lower than the time interval (5 min) of the ST layer. This means that the proposed HEMS can complete the optimization calculation within a set time interval.

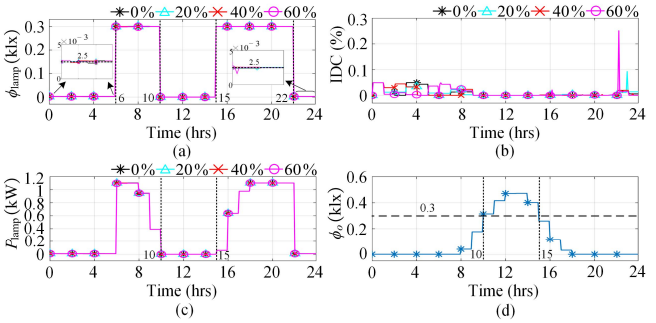

Fig. 8. Visual comfort in winter event: (a) Indoor illuminance generated by lamps, (b) Illuminance discomfort, (c) Lamps power usage, and (d) Indoor illuminance generated by sunlight.

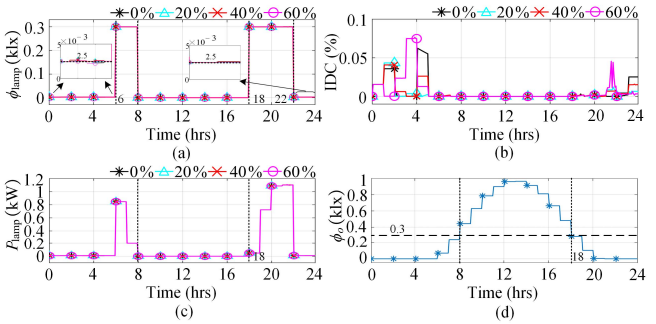

Fig. 9. Visual comfort in summer event: (a) Indoor illuminance generated by lamps, (b) Illuminance discomfort, (c) Lamps power usage, and (d) Indoor illuminance generated by sunlight.

TABLE IV
VISUAL COMFORT AND POWER PRICE UNDER DIFFERENT WEIGHTS

w_{vis}	J_{IDC}	Power cost ($)
0.01	0.0346	7.9384
0.05	0.0094	8.0461
0.1	0.0090	8.0599
0.5	0.0065	8.3601
1	0.0066	8.3830

C. *Visual Comfort*

This case study discusses the visual comfort under different errors. The visual comfort regulated by lamps in the residential house. When the indoor illuminance generated by outdoor sunlight exceeds the predefined illuminance, the lamps light will stop working. The case consists of winter and summer scenarios. As observed from Figs. 8(a) and 8(d), the indoor illuminance in winter can reach the set values at 0:00-6:00 and 6:00-10:00, which are 0.0025 klx and 0.3 klx, respectively. Then, the lamps do not participate in the adjustment of indoor illuminance from 10:00 to 15:00. This is because the indoor illuminance converted from outdoor sunlight exceeds the preset value of 0.32 klx. After that, the indoor illuminance is adjusted again by the lamps due to the decrease in indoor illuminance generated by outdoor sunlight. From Figs. 8(b) and 8(c), The proposed discomfort index approach under different error rates can uniformly limit different illuminance demands between 0 and 1. Besides, the IDC tends to be zero. This means that the users' visual comfort level becomes higher. Although the IDC has an extreme value at 40% and 60% errors, they are acceptable. The HEMS will adjust the power of lamps according to outdoor sunlight to satisfy the visual comfort of occupants at different time periods.

From Fig. 9, the HEMS can adjust the power usage of lamps according to summer indoor illuminance conditions under

different forecasting errors to meet the user's different visual comfort requirements. The IDC value approaches zero, which indicates a high visual comfort. In addition, it is obvious that the power consumption of lamps in winter is higher than in summer, as shown in Figs. 8(c) and 9(c). This is because the sunshine hours in summer are higher than that in winter. Therefore, the proposed HEMS can respond to seasonal changes to adjust the indoor illuminance to meet the needs of users.

Table IV illustrates the variations in visual comfort and electricity cost under different visual weight. When the visual weight is selected as 0.01, the visual discomfort is equal to 0.0346, and the daily electricity cost is $ 7.9384. When the weight is 1, the visual discomfort decreases to 0.0066, the power cost rises $ 8.3830. In general, as the visual weight increases, the user's visual discomfort tends to decrease, but the power cost increases.

D. Thermal Comfort

This case study will show the thermal comfort under different forecasting errors, which includes winter and summer scenarios. From Fig. 10(a), the indoor temperature in winter shows an upward trend at 0:00-3:00 and finally reaches the preset value of 22 ℃. This means that CAC consumes a lot of power to improve room temperature during this period, as shown in Fig. 10(c). Then, the indoor temperature can be maintained around 22 ℃ between 3:00 and 24:00. It can be observed from Fig. 10(b) that the TDC is very close to zero. This indicates a high level of thermal comfort for occupants. From Fig. 10(d), the outdoor temperature rises between 8:00 and 14:00, when the CAC slowly reduces the power consumption. After that, the outdoor temperature gradually decreases, and the power consumption of the CAC begins to increase again. This shows that the proposed HEMS can timely control the operation of CAC according to outdoor temperature conditions to meet the thermal comfort of users. In addition, different errors do not have any negative impact on thermal comfort regulation.

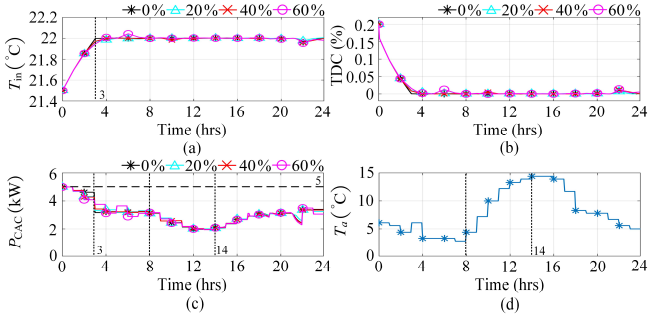

Fig. 10. Thermal comfort in winter event: (a) Indoor temperature, (b) Temperature discomfort, (c) CAC power usage, and (d) Outdoor temperature.

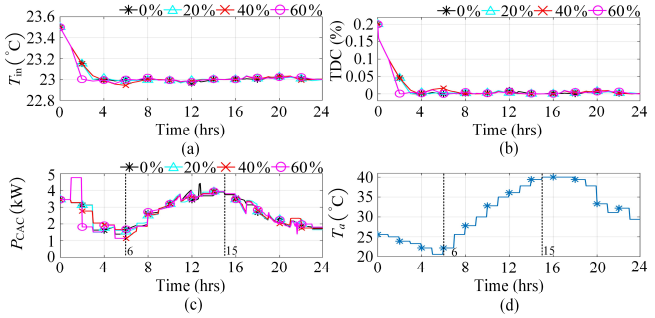

Fig. 11. Thermal comfort in summer event: (a) Indoor temperature, (b) Temperature discomfort, (c) CAC power usage, and (d) Outdoor temperature.

TABLE V
THERMAL COMFORT AND POWER PRICE UNDER DIFFERENT WEIGHTS

w_{ther}	J_{TDC}	Power cost ($)
0.01	0.4197	6.0447
0.05	0.0427	7.6626
0.1	0.0211	8.0599
0.5	0.0102	8.3996
1	0.0101	8.4377

Similar to the winter scenario, the proposed HEMS is able to adjust the indoor temperature to a set point in summer under different error rates, and the TDC is very close to zero, as shown in Figs. 11(a) and 11(b). As can be seen from Figs. 11(c) and 11(d), outdoor temperature rises between 6:00 and 15:00. The CAC needs to consume more power to guarantee the indoor temperature comfort. In general, the proposed HEMS can effectively guarantee the users' thermal comfort in different seasons.

Table V shows the relationship between thermal comfort and power cost under different weight. When the thermal weight is 0.01, the thermal discomfort and power cost are 0.4197 and $ 6.0447, respectively. When the weight factor is increased to 1, thermal discomfort decreases and the electricity bill increases. This means that the increase in thermal weight will elevate the power consumption of the temperature control device, thereby ensuring the user's thermal comfort.

E. Accurate Power Sharing and SoC Balance

This case studies the performance of the advanced voltage regulator. The batteries deliver different power between 0 and 4 s due to the different line resistances, as shown in Fig. 12(a). At 4 s, the accurate power-sharing control is added to the system. Then, the output power of the batteries reaches a consistent state at 4.3 s. From Fig. 12(b), the input voltages of the three batteries are 150 V, 100 V and 50 V, respectively. The bus voltage is not affected by different battery input voltages, it can still be maintained within the desired range (220 × (1 ± 5%) V). This is because the bus voltage is mainly dominated by the SC converter. From Fig. 12(c), the initial SoCs of the three batteries are set to 90%, 80% and 70%. Obviously, $SoC_{b,1}$ has the highest drop rate, while $SoC_{b,3}$ has the lowest drop rate. This means that the b,1 (battery - 1) provides the most output power, while the b,3 supplies the least output power. Therefore, the SoCs' gap among the batteries will gradually become smaller. From Fig. 12(d), the initial SoCs of the batteries are 30%, 20% and 10%. The batteries are operated in charging mode. $SoC_{b,3}$ rises faster than $SoC_{b,1}$ and $SoC_{b,2}$, while $SoC_{b,1}$ rises slower than $SoC_{b,2}$ and $SoC_{b,3}$. Hence, SoC balance among batteries can be achieved. Overall, the performance of the proposed advanced voltage regulator meets the expected requirements.

The performance of advanced voltage regulators with different battery capacities is also tested. The capacities of the b_1, b_2 and b_3 are set to 0.1 Ah, 0.08 Ah and 0.06 Ah, respectively. From Fig. 13(a) and 13(b), the initial SoCs of the three batteries are 90 %, 80 % and 70 %. The batteries are operated in discharging mode. The output power of a high-capacity battery (b_1) surpasses that of a low-capacity battery (b_3). Then, the SoC discrepancy among them gradually decreases, eventually reaching consistency. From Fig. 13(c) and 13(d), the initial

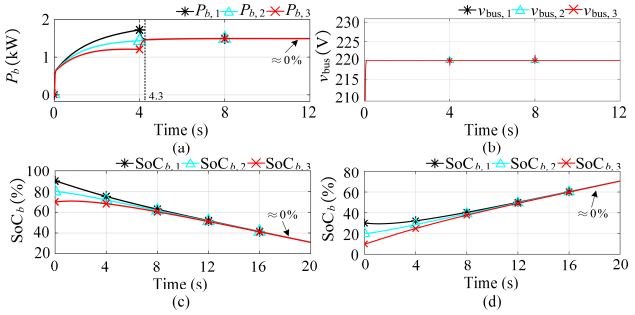

Fig. 12. Advanced voltage regulator: (a) Accurate power-sharing, (b) Bus voltages, (c) SoC balance in discharging mode, and (d) SoC balance in charging mode.

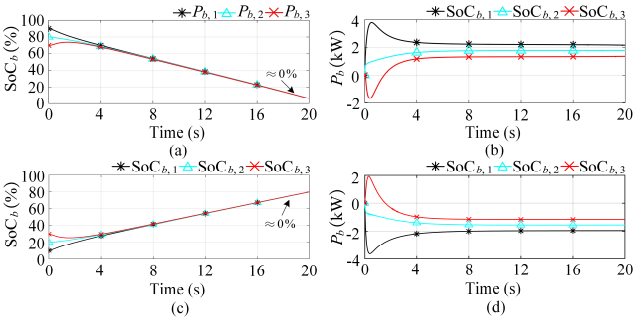

Fig. 13. Advanced voltage regulator with different capacity: (a) SoC balance in discharging mode, (b) Output power of batteries in discharging mode, (c) SoC balance in charging mode, and (d) Output power of batteries in charging mode.

SoCs of the batteries are set to 10%, 20% and 30%. Similar to the discharging mode, the SoC of the batteries can reach consistency under the charging mode. This indicates that the proposed method can ensure the SoC balance among the batteries regardless of the capacity differences.

F. Multi-Level HEMS Simulations

Case F will analyze the interaction between system-level and local-level HEMSs. It consists of two sub-cases: 1) power tracking capability of the local-level HEMS; 2) the operational status of the system under plug-and-play (PnP), and communication failure between the system-level and local-level HEMS. The initial values of the batteries' SoC are set at 60%, 50%, and 40% respectively, while the initial values of SCs' SoC are set at 50%. From Fig. 14(a), the battery b_1 with a higher SoC provides more power to the system than the one with a lower SoC between 0 to 2 h. The SoC balance among batteries is implemented regardless of the system line resistance. During the SoC balancing period, the battery cells will not adhere to the power scheduling plan provided by ST layer. Once the SoC balancing is completed, the battery cells will adjust according to the power reference. Furthermore, the local HEMS will regulate the total power of the battery in accordance with the reference power, as shown in Fig. 14(b). Similar to batteries, the output power of SCs can track the power decisions provided by the ST layer, as shown Fig. 14(c) and 14(d). Overall, the proposed local-level HEMS can effectively track power scheduling provided by system-level HEMS.

From Fig. 15(a), the SoC of the batteries is completed between 0 and 2 h. At 15 h, b_3 is disconnected from the system. Hence, it cannot provide power. The multi-layer EMS will detect the overall reduction in battery capacity and will

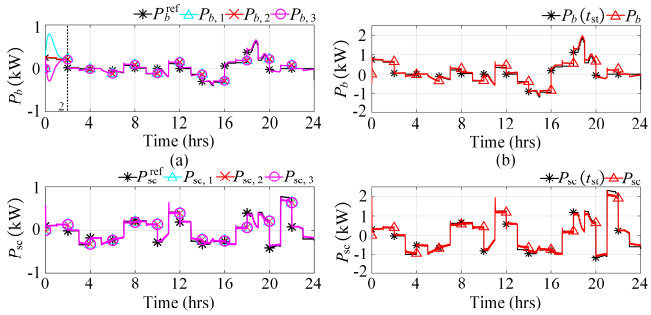

Fig. 14. Power tracking: (a) The output power of the battery, (b) The total power of the battery, (c) The power of the SC, and (d) The total power of the SC.

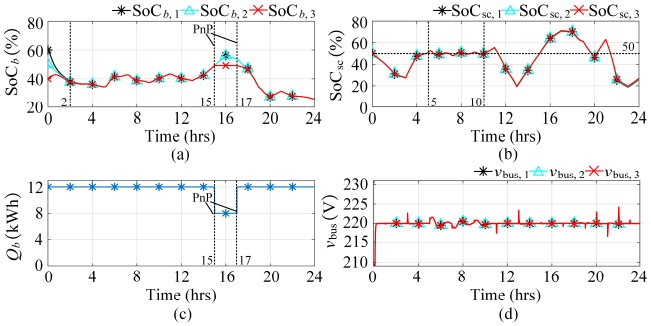

Fig. 15. The operational status of the system: (a) The SoC variations of the battery, (b) The SoC variations of the SC, (c) The capacity variations of the battery, and (d) DC bus voltages.

regenerate the power scheduling. At 17 h, b_3 is reconnected to the system to supply power, and the EMS will update the capacity information. Therefore, the proposed method can achieve the PnP mode, as shown in Fig. 15(a) and 15(c). Assume that within 6 to 10 h, a communication failure occurs between the system and the local HEMS. The local-level HEMS is unable to receive the reference information from system-level HEMS, and thus it automatically achieves power sharing between battery and SC through *v-dP* and *v-P* droop controls. The SC voltage recovery control in the local-level HEMS will ensure that the SoC of SCs fluctuates around the preset value 50%, as shown in Fig. 15(b). During this period, the DC bus voltage can be maintained within the desired range (220 × (1 ± 5%) V), as shown in Fig. 15(d). In summary, the proposed local-level HEMS can achieve autonomous power distribution and ensure voltage stability in emergency event.

G. Economic Analysis

In this case, the cash payback period is adopted to evaluate investment returns. Four group of methods will be discussed in detail: 1) The first group presents the proposed method; 2) The second group is from methods [24] and [25]; 3) The second group considers the proposed method that only takes into account the electricity cost, ignoring the storage degradation cost and user comfort; 3) The fourth group is Method III in Case B. The simulated data is listed in Table VI. It is evident that the electricity costs in Group IV are significantly higher than Group I - III. The absence of PV and HESS in Group IV leads to an increased reliance on the main power grid, thereby elevating electricity costs. In addition, the degradation cost of SC in Group I is higher than that in Group II and III. This indicates that the utilization rate of SC in Group I is higher. Furthermore, this will lead to a significantly lower battery degradation cost in

TABLE VI
Energy Cost Savings

Groups	I	II	III	IV
Battery cost ($)	53.6336	61.1669	180.4043	N/A
SC cost ($)	7.0376	7.0008	5.6591	N/A
Total cost ($)	2283.2272	2557.2935	1579.2025	3632.6623
Cost saving ($)	1349.4351	1075.3688	2053.4598	N/A
Payback periods (Years)	6.8	8.5	4.4	N/A

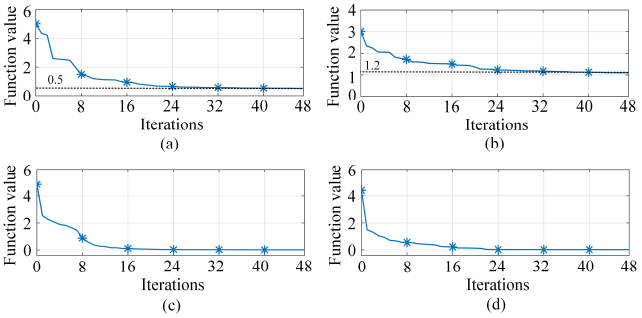

Fig. 16. Convergency discussions: (a) The convergency of LT layer at 12:00, (b) The convergency of LT layer at 17:00, (c) The convergency of ST layer at 10:40, and (d) The convergency of ST layer at 18:40.

Group I compared to Group II and III, thereby extending the lifespan of the battery. Additionally, since there is more optimization conditions considered in Group I and II, its overall electricity cost is inevitably higher than that of Group III. According to Table I, the total investment cost of the proposed HEMS is 9220 $. The cash payback period is equal to the total investment cost divided by the cost saving. Under the same conditions, the payback period for Group I is 6.8 years, which is significantly shorter than that of Group II. This indicates that the proposed method demonstrates superior performance. Due to the limited optimization conditions of Group III, its payback period is 4.4 years. Currently, the lifespan of PV can reach up to 25 years, while the service life of batteries and SC can reach up to 15 years [37]. This means that users can achieve net profit after 6.8 years. With the continuous decline in PV and HESS prices, the cash payback period becomes shorter [1]. Hence, the proposed HEMS is feasible.

H. Convergency Analysis

This case study focuses on the convergence of the proposed method under the solver "FMINCON". To verify the convergence of multi-time scale optimization, four time points are randomly selected: the times for the LT layer are 12:00 and 17:00, and the times for the ST layer are 10:40 and 18:40. It can be seen from Fig. 16(a) and 16(b) that the function value approaches a stable value after approximately 24 iterations of LT layer optimization. At 10:40, the ST layer only needs 16 iterations to make the function value approach zero, and it needs 24 iterations at 18:40, as shown in Fig. 16(c) and 16(d). Furthermore, the LT and ST optimization models exhibit fewer iterations when utilizing the solver "FMINCON". This indicates a faster convergence rate, thus achieving the predetermined expectations. It is important to note that this article focuses on the research of multi-level HEMS models rather than the development of solver algorithms. Therefore, the comparative performance of the solver's convergence is beyond the scope of this study.

VI. Conclusion and Future Work

In this article, a multi-level HEMS is proposed for minimization of the operating cost and the user discomfort in a DC home microgrid. The multi-level HEMS consists of a system-level and local-level HEMS. In the system-level HEMS, the LT layer is proposed to minimize the operating cost and the user discomfort. The ST is presented to mitigate the microgrid operating cost caused by randomness of user behavior and intermittent PV generation. The visual and thermal discomfort model is used to quantify the user comfort at different scenarios. Besides, the battery and SC degradation models are integrated into the HEMS to assess the wear cost. In the local-level HEMS, an advanced voltage regulator is proposed to achieve accurate power sharing and SoC balance among batteries. The power sharing between battery and SC is achieved by using coordinated droop controls. The DC bus voltage and SC voltage can be restored within a safe range. Future research work is to develop a coordination algorithm for home-home and home-grid energy exchange in energy markets.

References

[1] REN21, "Renewables 2022 global status," REN21, Paris, 2022. [Online]. Available: https://www.ren21.net/gsr-2022/.

[2] K. Vatanparvar and M. A. Al Faruque, "Design space exploration for the profitability of a rule-based aggregator business model within a residential microgrid," *IEEE Trans. Smart Grid*, vol. 6, no. 3, pp. 1167–1175, 2015, doi: 10.1109/TSG.2014.2380318.

[3] A. Chub, D. Vinnikov, E. Liivik, and T. Jalakas, "Multiphase quasi-Z-source DC-DC converters for residential distributed generation systems," *IEEE Trans. Ind. Electron.*, vol. 65, no. 10, pp. 8361–8371, 2018, doi: 10.1109/TIE.2018.2801860.

[4] M. Beaudin, H. Zareipour, A. Kiani Bejestani, and A. Schellenberg, "Residential energy management using a two-horizon algorithm," *IEEE Trans. Smart Grid*, vol. 5, no. 4, pp. 1712–1723, Jul. 2014, doi: 10.1109/TSG.2014.2310395.

[5] Y. Liu, Y. Zhang, K. Chen, S. Z. Chen, and B. Tang, "Equivalence of multi-time scale optimization for home energy management considering user discomfort preference," *IEEE Trans. Smart Grid*, vol. 8, no. 4, pp. 1876–1887, 2017, doi: 10.1109/TSG.2015.2510222.

[6] A. Anvari-Moghaddam, H. Monsef, and A. Rahimi-Kian, "Optimal smart home energy management considering energy saving and a comfortable lifestyle," *IEEE Trans. Smart Grid*, vol. 6, no. 1, pp. 324–332, 2015, doi: 10.1109/TSG.2014.2349352.

[7] M. Rastegar, "Impacts of residential energy management on reliability of distribution systems considering a customer satisfaction model," *IEEE Trans. Power Syst.*, vol. 33, no. 6, pp. 6062–6073, 2018, doi: 10.1109/TPWRS.2018.2825356.

[8] R. Teng and T. Yamazaki, "Load profile-based coordination of appliances in a smart home," *IEEE Trans. Consum. Electron.*, vol. 65, no. 1, pp. 38–46, 2019, doi: 10.1109/TCE.2018.2885874.

[9] F. Wang *et al.*, "Multi-objective optimization model of source-load-storage synergetic dispatch for a building energy management system based on TOU price demand response," *IEEE Trans. Ind. Appl.*, vol. 54, no. 2, pp. 1017–1028, 2018, doi: 10.1109/TIA.2017.2781639.

[10] S. Aznavi, P. Fajri, A. Asrari, and F. Harirchi, "Realistic and intelligent management of connected storage devices in future smart homes considering energy price tag," *IEEE Trans. Ind. Appl.*, vol. 56, no. 2, pp. 1679–1689, 2020, doi: 10.1109/TIA.2019.2956718.

[11] A. Chatterjee, S. Paul, and B. Ganguly, "Multi-objective energy management of a smart home in real time environment," *IEEE Trans. Ind. Appl.*, vol. 59, no. 1, pp. 138–147, 2023, doi: 10.1109/TIA.2022.3209170.

[12] M. Shafie-Khah and P. Siano, "A stochastic home energy management system considering satisfaction cost and response fatigue," *IEEE Trans. Ind. Informatics*, vol. 14, no. 2, pp. 629–638, 2018, doi: 10.1109/TII.2017.2728803.

[13] Y. Zhang, R. Wang, T. Zhang, Y. Liu, and B. Guo, "Model predictive control-based operation management for a residential microgrid with considering forecast uncertainties and demand response strategies," *IET*

Gener. Transm. Distrib., vol. 10, no. 10, pp. 2367–2378, 2016, doi: 10.1049/iet-gtd.2015.1127.
[14] L. Bhamidi and S. Sivasubramani, "Optimal planning and operational strategy of a residential microgrid with demand side management," *IEEE Syst. J.*, vol. 14, no. 2, pp. 2624–2632, 2020, doi: 10.1109/JSYST.2019.2918410.
[15] S. Sharma, A. Verma, Y. Xu, and B. K. Panigrahi, "Robustly coordinated bi-level energy management of a multi-energy building under multiple uncertainties," *IEEE Trans. Sustain. Energy*, vol. 12, no. 1, pp. 3–13, 2021, doi: 10.1109/TSTE.2019.2962826.
[16] M. Elkazaz, M. Sumner, E. Naghiyev, S. Pholboon, R. Davies, and D. Thomas, "A hierarchical two-stage energy management for a home microgrid using model predictive and real-time controllers," *Appl. Energy*, vol. 269, no. February, p. 115118, 2020, doi: 10.1016/j.apenergy.2020.115118.
[17] D. Yassuda Yamashita, I. Vechiu, and J. P. Gaubert, "Two-level hierarchical model predictive control with an optimised cost function for energy management in building microgrids," *Appl. Energy*, vol. 285, no. November 2020, p. 116420, 2021, doi: 10.1016/j.apenergy.2020.116420.
[18] D. Watari *et al.*, "Multi-time scale energy management framework for smart PV systems mixing fast and slow dynamics," *Appl. Energy*, vol. 289, no. February, p. 116671, 2021, doi: 10.1016/j.apenergy.2021.116671.
[19] X. Jin, J. Wu, Y. Mu, M. Wang, X. Xu, and H. Jia, "Hierarchical microgrid energy management in an office building," *Appl. Energy*, vol. 208, no. July, pp. 480–494, Dec. 2017, doi: 10.1016/j.apenergy.2017.10.002.
[20] F. Luo, G. Ranzi, S. Wang, and S. Member, "Hierarchical energy management system for home microgrids," *IEEE Trans. Smart Grid*, vol. 10, no. 5, pp. 5536–5546, 2019.
[21] P. Zhuang, H. Liang, and M. Pomphrey, "Stochastic multi-timescale energy management of greenhouses with renewable energy sources," *IEEE Trans. Sustain. Energy*, vol. 10, no. 2, pp. 905–917, 2019, doi: 10.1109/TSTE.2018.2854662.
[22] M. C. Argyrou, C. C. Marouchos, S. A. Kalogirou, and P. Christodoulides, "A novel power management algorithm for a residential grid-connected PV system with battery-supercapacitor storage for increased self-consumption and self-sufficiency," *Energy Convers. Manag.*, vol. 246, p. 114671, 2021, doi: 10.1016/j.enconman.2021.114671.
[23] S. Kumar, A. Agrawal, and R. Gupta, "Power balance for WTG - solar PV fed DC microgrids with battery and supercapacitor support," *Proc. 2018 IEEE Int. Conf. Power Electron. Drives Energy Syst. PEDES 2018*, no. 24, pp. 1–6, 2018, doi: 10.1109/PEDES.2018.8707703.
[24] C. Ju, P. Wang, L. Goel, and Y. Xu, "A two-layer energy management system for microgrids with hybrid energy storage considering degradation costs," *IEEE Trans. Smart Grid*, vol. 9, no. 6, pp. 6047–6057, 2018, doi: 10.1109/TSG.2017.2703126.
[25] J. He, C. Shi, T. Wei, X. Peng, and Y. Guan, "Hierarchical optimal energy management strategy of hybrid energy storage considering uncertainty for a 100% clean energy town," *J. Energy Storage*, vol. 41, no. May, p. 102917, 2021, doi: 10.1016/j.est.2021.102917.
[26] A. Anvari-Moghaddam, J. M. Guerrero, J. C. Vasquez, H. Monsef, and A. Rahimi-Kian, "Efficient energy management for a grid-tied residential microgrid," *IET Gener. Transm. Distrib.*, vol. 11, no. 11, pp. 2752–2761, 2017, doi: 10.1049/iet-gtd.2016.1129.
[27] Y. Fujimoto *et al.*, "Distributed energy management for comprehensive utilization of residential photovoltaic outputs," *IEEE Trans. Smart Grid*, vol. 9, no. 2, pp. 1216–1227, 2018, doi: 10.1109/TSG.2016.2581882.
[28] M. Bahloul, L. Breathnach, and S. Khadem, "Design and Field Implementation of a Hierarchical Control Solution for Residential Energy Storage Systems," *IEEE Trans. Smart Grid*, vol. 14, no. 2, pp. 1083–1092, 2023, doi: 10.1109/TSG.2022.3198224.
[29] P. R. Michael, D. E. Johnston, and W. Moreno, "A conversion guide: Solar irradiance and lux illuminance," *J. Meas. Eng.*, vol. 8, no. 4, pp. 153–166, 2020, doi: 10.21595/jme.2020.21667.
[30] X. Lin, R. Zamora, C. Baguley, and A. K. Srivastava, "A hybrid short-term load forecasting approach for individual residential customer," *IEEE Trans. Power Deliv.*, vol. 38, no. 1, pp. 26–37, 2023, doi: 10.1109/TPWRD.2022.3178822.
[31] P. Kreczanik, P. Venet, A. Hijazi, and G. Clerc, "Study of supercapacitor aging and lifetime estimation according to voltage, temperature, and RMS current," *IEEE Trans. Ind. Electron.*, vol. 61, no. 9, pp. 4895–4902, 2014, doi: 10.1109/TIE.2013.2293695.
[32] F. Zheng, Y. Li, and X. Wang, "Study on effects of applied current and voltage on the ageing of supercapacitors," *Electrochim. Acta*, vol. 276, pp. 343–351, 2018, doi: 10.1016/j.electacta.2018.04.153.
[33] X. Lin, R. Zamora, and C. A. Baguley, "A comprehensive multi-functional controller for hybrid energy storage systems in DC microgrids," *IEEE Trans. Ind. Appl.*, vol. 59, no. 1, pp. 2985–2994, 2023, doi: 10.1109/TIA.2023.3243601.
[34] Q. Xu, J. Xiao, X. Hu, P. Wang, and M. Y. Lee, "A decentralized power management strategy for hybrid energy storage system with autonomous bus voltage restoration and state-of-charge recovery," *IEEE Trans. Ind. Electron.*, vol. 64, no. 9, pp. 7098–7108, 2017, doi: 10.1109/TIE.2017.2686303.
[35] NREL, "End-use load profiles for the U.S. building stock," 2021. doi: https://dx.doi.org/10.25984/1876417.
[36] "Real-time pricing for residential customers," *Ameren Illinois Power Company*, 2012. https://www2.ameren.com/retailen- ergy/-realtimeprices.aspx (accessed Mar. 01, 2023).
[37] T. S. Babu, K. R. Vasudevan, V. K. Ramachandaramurthy, S. B. Sani, S. Chemud, and R. M. Lajim, "A comprehensive review of hybrid energy storage systems: converter topologies, control strategies and future prospects," *IEEE Access*, vol. 8, pp. 148702–148721, 2020, doi: 10.1109/ACCESS.2020.3015919.

Xin Lin received the B.S. in electrical engineering from Waikato Institute of Technology, Hamilton, New Zealand, in 2016, M.S. degree in electrical engineering from Auckland University of Technology, Auckland, New Zealand, in 2017, and Ph.D. in electrical engineering at Auckland University of Technology, Auckland, New Zealand, in 2023. Currently, he is a Lecturer with the Sanming University. His research interests include microgrids, intelligent energy management system, energy storage technology and power converter control.

Ramon Zamora received the Ph.D. degree in electrical engineering from Washington State University, Pullman, WA, USA, in 2015. He is a Lecturer with the Auckland University of Technology. His research interests include power system modeling, simulation and control, power system management and controls, power electronic application for power systems, grid integration of renewable energy and energy storage, microgrid and smart grid, and distributed controls.

Yazhou Jiang (S'12, M'17) earned his Ph.D. degree from Washington State University, Pullman, WA, in 2016. Currently he is an Assistant Professor at Clarkson University, Potsdam NY, and a Principal Engineer at Avangrid and RLC Engineering as a secondary appointment. Dr. Jiang was a Power Systems Engineer at the GE Global Research center, Niskayuna, NY from 2016-2020. His research interests include risk management in power grid operation, renewable integration, and data analytics for power system applications.

Gang Chen received the B. S. in vehicle engineering from Jiamusi University, Jiamusi, China, in 2009, M.S. degree in vehicle engineering from Chang'an University, Chang'an, China, in 2012, and the Ph.D. degree in mechanical engineering from Fuzhou University, Fuzhou, China, in 2021. Currently, he is a Professor at School of Mechanical and Electrical Engineering at the Sanming University. His research interests include electrical vehicle, electrical machine technology and battery management system.

Anurag K. Srivastava is a Raymond J. Lane Professor and Chairperson of the Computer Science and Electrical Engineering Department at the West Virginia University. He is also an adjunct professor at the Washington State University and senior scientist at the Pacific Northwest National Lab. He received his Ph.D. degree in electrical engineering from the Illinois Institute of Technology in 2005. His research interest includes data-driven algorithms for power system operation and control including resiliency analysis. In past years, he has worked in a different capacity at the Réseau de transport d´électricité in France; RWTH Aachen University in Germany; PEAK Reliability Coordinator, Idaho National Laboratory, PJM Interconnection, Schweitzer Engineering Lab (SEL), GE Grid Solutions, Massachusetts Institute of Technology and Mississippi State University in USA; Indian Institute of Technology Kanpur in India; as well as at Asian Institute of Technology in Thailand. He is serving as chair of the IEEE Power & Energy Society's (PES) PEEC committee, co-chair of the microgrid working group, vice-chair of power system operation SC, chair of PES voltage stability working group, chair of PES synchrophasors applications working group, co-chair of distributed optimization application in power grid, vice-chair of tools for power grid resilience TF, and member of CIGRE C4C2-58 Voltage Stability, C4.47/ C2.25 Resilience WG. He is the author of more than 300 technical publications including a book on power system security and 4 patents.